GROWTH AND CHARACTERIZATION OF $CuIn_{1-x}Ga_xSe_2$ (CIGS) THIN FILMS FOR SOLAR CELL STRUCTURES

A THESIS SUBMITTED TO
THE GRADUATE SCHOOL OF NATURAL AND APPLIED SCIENCES
OF
MIDDLE EAST TECHNICAL UNIVERSITY

BY

İDRİS CANDAN

IN PARTIAL FULFILLMENT OF THE REQUIREMENTS
FOR
THE DEGREE OF MASTER OF SCIENCE
IN
PHYSICS

DECEMBER 2009

Approval of the thesis:

GROWTH AND CHARACTERIZATION OF $CuIn_{1-x}Ga_xSe_2$ (CIGS) THIN FILMS FOR SOLAR CELL STRUCTURES

submitted by **İDRİS CANDAN** in partial fulfillment of the requirements for the degree of **Master of Science in Physics Department, Middle East Technical University** by,

Prof. Dr. Canan Özgen
Dean, Graduate School of **Natural and Applied Sciences** _____

Prof. Dr. Sinan Bilikmen
Head of Department, **Physics** _____

Prof. Dr. A.Çiğdem Erçelebi
Supervisor, **Physics Dept., METU** _____

Prof. Dr. Mehmet Parlak
Co-Supervisor, **Physics Dept., METU** _____

Examining Committee Members:

Prof. Dr. Raşit Turan
Physics Dept., METU _____

Prof. Dr. A.Çiğdem Erçelebi
Physics Dept., METU _____

Prof. Dr. Mehmet Parlak
Physics Dept., METU _____

Prof. Dr. İbrahim Günal
Physics Dept., METU _____

Prof. Dr. Macit Özenbaş
Metallurgical and Materials Engineering Dept., METU _____

Date: _____

I hereby declare that all information in this document has been obtained and presented in accordance with academic rules and ethical conduct. I also declare that, as required by these rules and conduct, I have fully cited and referenced all material and results that are not original to this work.

Name, Last name : İDRİS CANDAN

Signature :

ABSTRACT

GROWTH AND CHARACTERIZATION OF $CuIn_{1-x}Ga_xSe_2$ (CIGS) THIN FILMS FOR SOLAR CELL STRUCTURES

Candan, İdris

M.S., Department of Physics

Supervisor : Prof. Dr. A. Çiğdem Erçelebi

Co-Supervisor : Prof. Dr. Mehmet Parlak

December 2009, 78 pages

Direct conversion of solar energy, which is the most powerful and unlimited one among the renewable energy sources; into the electrical energy by the photovoltaic devices, is a promising way of meeting the energy needs of future. Thin film semiconductor materials show great promise for the production of efficient, low-cost solar cell devices. Recently advanced research on thin film photovoltaics in all aspects, has attracted intense attention. Thin film semiconductors for the photovoltaic applications are deposited in large areas by different methods.

In this study, deposition and characterization of $CuIn_{1-x}Ga_xSe_2$ *(CIGS)* semiconductor thin films by thermal evaporation and e-beam evaporation methods were investigated. Material properties and deposition parameters of the thin films are aimed to be optimized for solar cell applications. Structural properties of the deposited *CIGS* thin films were examined through X-ray diffraction and Energy Dispersive X-ray Analysis. The temperature dependent electrical conductivity, Hall effect and photoconductivity of these samples have been measured between 100 and

400 K. For the optical characterization of CIGS thin films, the transmission measurements have been carried out in the wavelength region of 325-900 nm. The changes in the structural, electrical and optical properties of samples through post-depositional annealing effect were also analyzed.

Keywords : CIGS, Thin film, Solar cell, Thermal evaporation, E-beam evaporation, Structural characterization, Electrical characterization, Optical characterization

ÖZ

GÜNEŞ PİLİ YAPILARI İÇİN $CuIn_{1-x}Ga_xSe_2$ (CIGS) İNCE FİLMLERİN BÜYÜTÜLMESİ VE KARAKTERİZASYONU

Candan, İdris

Yüksek Lisans, Fizik Bölümü

Tez Yöneticisi : Prof. Dr. A. Çiğdem Erçelebi

Ortak Tez Yöneticisi : Prof. Dr. Mehmet Parlak

Aralık 2009, 78 sayfa

Yenilenebilir enerji kaynakları arasında en güçlü ve sonsuz olan güneş enerjisinin fotovoltaik aygıtlar ile doğrudan elektrik enerjisine dönüştürülebilmesi, bu yolla enerji ihtiyacının karşılanabilmesinin yolunu açmış, ucuz ve yüksek verimli güneş pillerinin elde edilmesine yönelik Ar-Ge çalışmaları önem kazanmıştır. İnce film yarıiletken malzemeler kullanılarak üretilen fotovoltaik aygıtlar, esnek tabanlar üzerine, daha az malzeme ve ucuz yöntemlerle elde edilebilme özelliklerinden ötürü yoğun olarak çalışılan, güncel araştırma konusudur. Fotovoltaik aygıtlar için ince filmleri değişik yöntemler kullanarak elde etmek mümkün olmaktadır.

Bu çalışmada $CuIn_{1-x}Ga_xSe_2$ *(CIGS)* yarıiletken ince filmlerin ısısal ve elektron demeti buharlaştırma teknikleri kullanılarak elde edilmesi, güneş pili yapıları için gerekli malzeme özelliklerinin araştırılması amaçlanmaktadır. Üretilen filmlerin karakterize edilerek özelliklerinin güneş pili uygulamaları için optimize edilmesi, çalışmanın amaçları arasındadır. Üretilmis *CIGS* filmlerin yapısal

özellikleri X-ışını kırınımı ve enerji dağılımlı X-ışınları analizi yöntemleri ile incelendi. Sıcaklık bağımlı elektriksel iletkenlik, Hall etkisi ve fotoiletkenlik ölçümleri 100 ile 400 K aralığında yapıldı. Filmlerin optik karakterizasyonu için 325-900 nanometre dalgaboyu aralığında geçirgenlik ölçümleri gerçekleştirildi. CIGS ince filmlerde yapı, elektrik ve optik özelliklerin üretim sonrası uygulanan ısıl işlem ile değişimi de çalışıldı.

Anahtar Kelimeler: CIGS, İnce film, Güneş pili, Isısal buharlaştırma, Elektron demeti ile buharlaştırma, Yapısal karakterizasyon, Elektriksel karakterizasyon, Optiksel karakterizasyon

To All Member's of My Lovely Family

ACKNOWLEDGEMENTS

It is a great pleasure to work with my supervisor Prof. Dr. A.Çiğdem Erçelebi. Her valuable patience, encouragement and support led to the completion of the thesis. I always feel an admiration about her positive energy, scientific knowledge and creative criticism throughout thesis.

I express my endless thanks to my co-supervisor Prof. Dr. Mehmet Parlak for his scientific guadience, helpful suggestions, keeping his eyes on me at every steps of experimental stages, continous support and kind friendship.

I would like to thank to my current lab-mates Dr. Tahir Çolakoğlu, Hakan Karaağaç, Murat Kaleli and Hasan Hüseyin Güllü for their helps and friendship.

I also would like to thank to Mustafa Kulakçı and Yücel Eke for his kind friendship and for their technical assistance.

I wish to thank my friends: Dr. M. Ali Kaplan, Olcay Mert, Muhammed Aydın, Nevfel Boz, Fahri Öztürk, Cevdet Bayar, Çağaçan Değer, Önder Gülbeyaz, Yasin Tunç, Seda Musaoğlu, Hüseyin Kırmızı, İlker Kılıç and Ceren Coşkun.

My special thanks go to my parents, Nesibe and Muhiddin Candan, my brothers and sisters, for their endless love. They are always with me and have supported endlessly me whenever I need them.

TABLE OF CONTENTS

LIST OF TABLES

TABLES

LIST OF FIGURES

FIGURES

CHAPTER 1

INTRODUCTION

"Thin-film technology is simultaneously one of the oldest arts and one of the newest sciences" [1].

Solar photovoltaic technology is a promising alternative energy source to meet the world energy demand because it harvests energy from the sun. 174 petawatts of incoming solar radiation reaches to the earth at the upper atmosphere at any given time [2]. This cited value is more than all the energy that could be used by all humans in the world for an entire year [3]. After acrossing the earth's atmosphere, nearly half the isolation is the visible electromagnetic spectrum and the other half mostly in the infrared spectrum and a small part is ultraviolet radiation. This energy drives climate and supports all life on Earth.

Solar energy is used synonymously with solar power and sometimes more specifically to refer to the transformation of sunlight into electricity. This can be done via photovoltaic effect or by heating a transmission of fluid to produce vapor to run a generator. Solar cell device is used to convert sunlight into electricity. Basically, solar cell depends on photon absorbtion and the following generation of electron-hole pairs in the semiconductor material. A solar cell is fundamentally a p-n junction diode. When semiconductors absorb light that has energy greater than bandgap energy, electron-hole pairs are created, the created carriers are separated by the internal electric field at the p-n junction and are collected by the contacts.

Photovoltaics may be regarded as space-age technology, but it is a technology that in fact has been around for quite some time. The photovoltaic effect was first reported by French physicist Edmond Bacquerel in 1839[4]. In one of electrical workout, he placed two plates in a conductive fluid, and when he exposed the setup to the sunlight incidentally he observed a small voltage. Nearly 40 years later, in 1873 English physicist Willoughby Smith discovered that selenium was sensitive to light[5]. Light struck selenium and electrical current is generated. The first working solar cell was constructed by Charles Fritts in 1886. These prototype cells were made of selenium and achieved efficiencies around 1 %. In an early publication Fritts expressed that one of the great advantage of solar cell is that " *the supply of solar energy is both without limit and without cost, and will continue to stream down on earth after we exhaust our supplies of fossil fuels*" [6].

The first generation of solar cells are silicon wafer-based solar cells. Finally it would be replaced by a second generation of lower cost thin-film based solar cell technology involving a different semiconductor. CdS, a:Si (amorphous silicon), CdTe, $CuIn_{1-x}Ge_xSe_2$ and thin-film poly:Si (polycrystalline silicon) have been regarded as thin-film solar cell candidates.

Thin film cells are deposited directly onto glass, stainless steel or plastic substrates. Conversion efficiencies for commercial photovoltaic modules range from 8% to 15 % depending on type of material and fabrication method.

Today, photovoltaics are likely to evolve, in its most mature form, to a third generation of high efficiency thin film solar cell technology. These new devices contain photochemical cells, polymer solar cells, tandem cells, nanocrystal solar cells and are still in the research phase.

The focus of this study is to investigate the growth and characterization of $CuIn_xGa_{1-x}Se_2$ (CIGS) thin films towards the production of high efficiency photovoltaic devices. Polycrystalline chalcopyrite $CuIn_{1-x}Ga_xSe_2$ (CIGS) thin films were obtained by different growth techiques and structural, electrical and optical properties of deposited films were studied in detail.

The reason why the researcher chose to use this thin chalcopyrite polycrystalline film is that it is cheap; its components are readily available; it does not require very much advanced technological methods to produce it. Also, it can be deposited onto cheap soda-lime glass by different methods. Different techniques have been used to deposit CIGS thin films. CIGS based solar cells have shown efficiencies with no evidence of reduction of the absorber layer with time or light exposure. They showed excelent radiation hardness under irradiation [7].

Polycrystalline chalcopyrite $CuIn_{1-x}Ga_xSe_2$ (CIGS) thin films are used as the absorber layer for the production of high efficiency sollar cells. A variety of theoretical and experimental studies have been performed in order to investigate their properties. Quaternary ($CuIn_{1-x}Ga_xSe_2$) compound materials have been grown on various substrates by different methods and techniques such as electron beam evaporation (e-beam evaporation) [8-10], reactive magnetron sputtering [11], thermal evaporation [12,13], thermal co-evaporation [14-16] , flash evaporation [17], pulsed laser deposition (PLD) [18,19] and physical vapor transport [20].

In 1994, K. Kushiya *et al* [16] used two-stage development method and reported to achive 14.9 % efficiency in the development of CIGS thin film. Today, conversion efficiency of 19.3 % has been achieved by K. Ramanathan *et al*. with the probability of yielding 20 % efficiency [9]. The optical nature, mobility/diffusion

length limitation, spatial variations of composition, band gap oscillations and stoichiometry of the chalcopyrite compound of $CuIn_{1-x}Ga_xSe_2$ are obstructions for it. Theoretically, 26 % efficiency would be possible if there were only band gap oscillations as far as scientists are concerned [21].

The optical, electrical and structural properties of $CuIn_{1-x}Ga_xSe_2$ (CIGS) thin film changes with different parameters such as Cu/(In+Ga) and Ga/(In+Ga) or In/(In+Ga) ratios and/or film thickness [7,10]. The components ratios, effect the absorption coefficient and band gap values also [7,10,13,15]. The measurements show that the optimum value of Ga/(In+Ga) ratio is between 25 and 30 [17]. X-ray diffraction (XRD) examination of the films at room temperature shows that diffraction peak around $2\theta=26.74°$ display a strong (112) preferred orientation [13,17,23]. The other peaks at $2\theta = 44.35°$, and 52.74° are caused by diffraction from the (220) plus (204), and the (312) planes, respectively. The small positive alteration in 2θ value of (112) peak for the CIGS films showed that gallium takes partly the place of indium in the tetragonal CIS phase and then results in the tetragonal CIGS phase [23].

Detailed studies have been performed on the optical properties of CIGS polycrystalline thin films. There are important differences in the electrical properties between stoichiometric CIS (x=0) and CGS (x=1). The researcher found that with increasing addition of Ga, the valence band maximum of $CuIn_{1-x}Ga_xSe_2$ (CIGS) decreases slightly, while the conduction band minimum increases as a consequence the band gap of CIGS enlarges significantly [24]. The band gap of $CuInSe_2$ (x=0) (CIS) and $CuGaSe_2$ (x=1) (CGS) is about 1 eV and 1.7 eV, respectively. Thus, the band gap of CIGS has a value between 1 eV and 1.7 eV with addition of gallium

[23]. Besides, thin layers of the CIGS are considered as the most promising material for low cost and high-efficiency solar cells, because of their high absorptivity ($>10^5 cm^{-1}$) and stability against photo-degradation [24].

According to the growth conditions, CIGS polycrystalline thin films can be both n-type and p-type. They normally have p- type electrical conduction. If more In and Ga are adjoined in the layers, the material shows n-type electrical conduction[22].

In this study, the detailed investigation of the structural, electrical and optical properties CIGS thin films, grown by the electron beam and thermal evaporation techniques using $CuIn_{0.5}Ga_{0.5}Se_2$ powder have been performed, by means of X-ray diffraction analysis, energy dispersive X-ray analysis (EDXA), and the temperature dependent conductivity measurements in the temperature range of 100-400 K. Systematic annealing procedure was applied to the the samples, to figure out the effect of post annealing on the physical, optical and electrical properties of the films.

This thesis is organized as follows: Chapter 2 introduces the basic concepts of the chalcopyrite polycrystalline CIGS thin films and confirms theoretical background for solar cell applications. Chapter 3 gives a description of the experimantal methods used for structural, electrical and optical measurements of CIGS thin films. Finally, Chapter 4 includes experimental results and gives explanation of these results. Besides, in this chapter, we will discuss conformity and/or disconformity between the experimental measurement results and theoretical argument.

CHAPTER 2

THEORETICAL CONSIDERATION

2.1. Physics of Solar Cell Device

There are several types of semiconductors: elemental (IV), binary compounds (I-VII , II-VI and III-V), ternary and multinary compounds (II-IV-V_2 , I-III-VI_2 ,etc.) oxides (Cu_2O, ZnO, La_2CuO_4 , etc.) and organic semiconductors. The best-known two elemental semiconductors are Si and Ge. The examples of well-known III-V compound semiconductors are GaAs, InP and GaN, and II-VI coumpound semiconductors are CdTe and ZnSe.

Semiconductors are classified as p-type and n-type depending on the majority carriers which are holes and electrons, respectively.

A solar cell device is used for the production of electricity from solar energy and it is basically a p-n junction diode. Electron-hole pairs are produced by the solar radiation when the semiconductor absorbs light with energy greater than its band gap. The produced carriers (electrons or holes) are separated by the electric field in the depletion region.

Solar cells are fundamentally semiconductor junctions under illumination. Electron-hole pairs are generated by light on both sides of the junction, in the p-type base and in the n-type emitter. The generated electrons and holes diffuse to the junction and are swept away by the electric field. Consequently, electric current produces across the device. The p-n junction separates the carriers with opposite

charge, and transforms the generation current between the bands inside an electric current across the p-n junction.

A solar cell consists of a back ohmic contact that cover the back surface, a shallow p-n junction on the surface, a front ohmic contact stripe, and an antireflection coating on the front surface. Schematic representation of p-n junction solar cell is shown in Figure 2.1 [25].

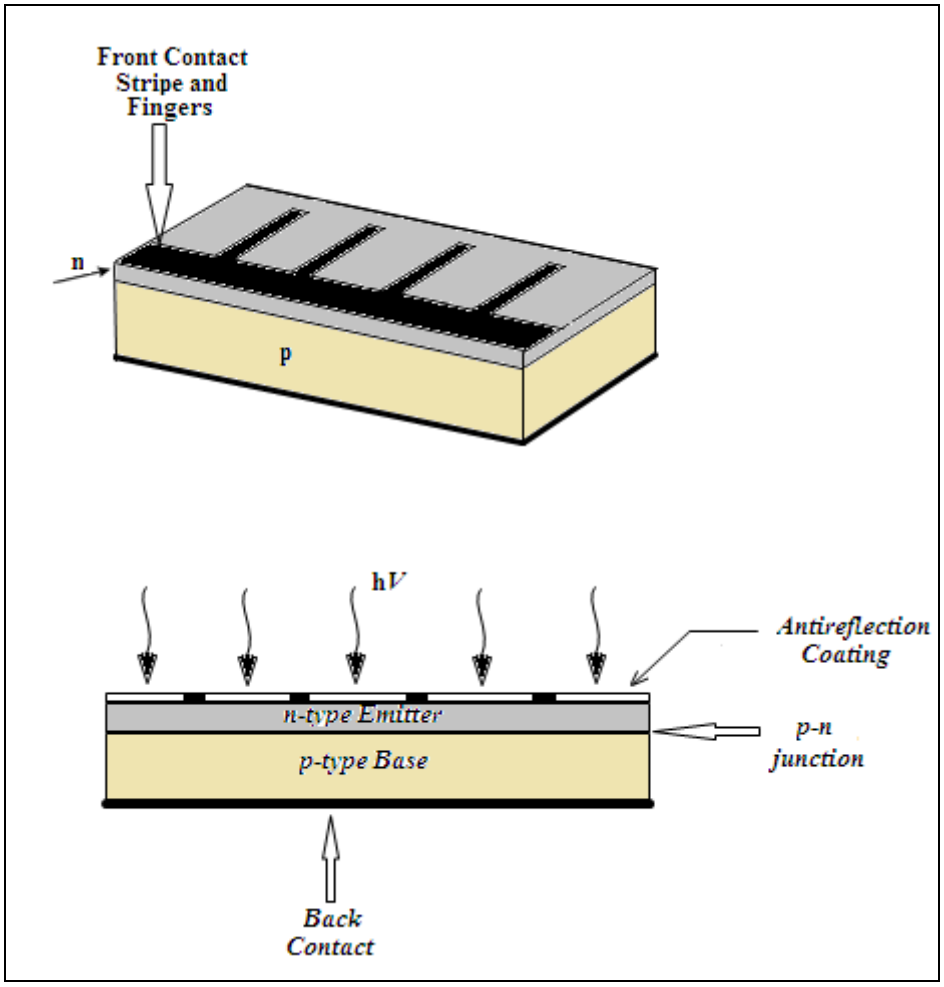

Figure 2.1 : Schematic representation of p-n junction solar cell [25].

2.1.1 Heterojunction

The CIGS-based solar cells is built up by several layers (glass/Mo/CIGS /CdS/and other layers) as shown in Fig. 2.2. The role of the glass is to support the solar cell structure, the role of the Mo layer is to form a good ohmic contact to the p-type CIGS layer. The CIGS layer itself is the main part of the solar cell, where the absorption of the solar radiation takes place. On top of the CIGS layer a n-type CdS buffer layer is deposited [26]. This buffer layer will play an important role in the formation of the heterojunction.

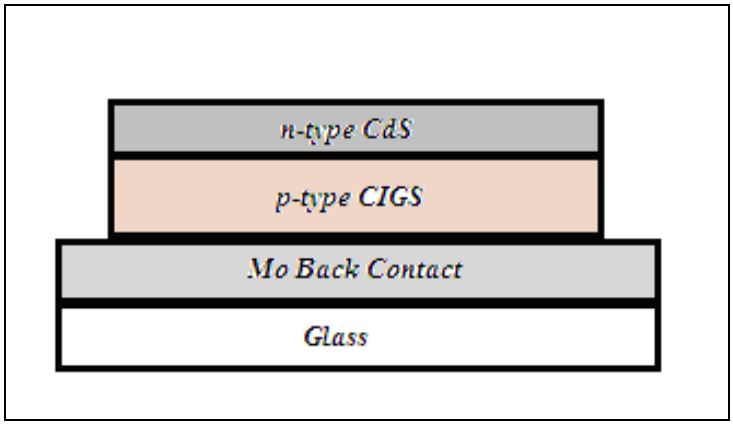

Figure 2.2 : Schematic illustration of the CIGS solar cell structure [27].

Heterojunction is a junction formed between two semiconductors. Since the semiconductor materials have different bandgap and electron affinities, in the valence band and conduction band discontinuities occur due to band bending. If these discontinuities are very large, they can oppositely affect the current flow as like they exist a barrier to the mobile charge carriers. The energy band diagram of

a representative heterojunction is shown in Figure 2.3. E_{g1}, Φ_1, V_{b1} and χ_1 are band gap, workfunction, built-in potential and electron affinities for p-type semiconductor, respectively. E_{g2}, Φ_2, V_{b2} and χ_2 are band gap, workfunction, built-in potential and electron affinities for n-type semiconductor, respectively.

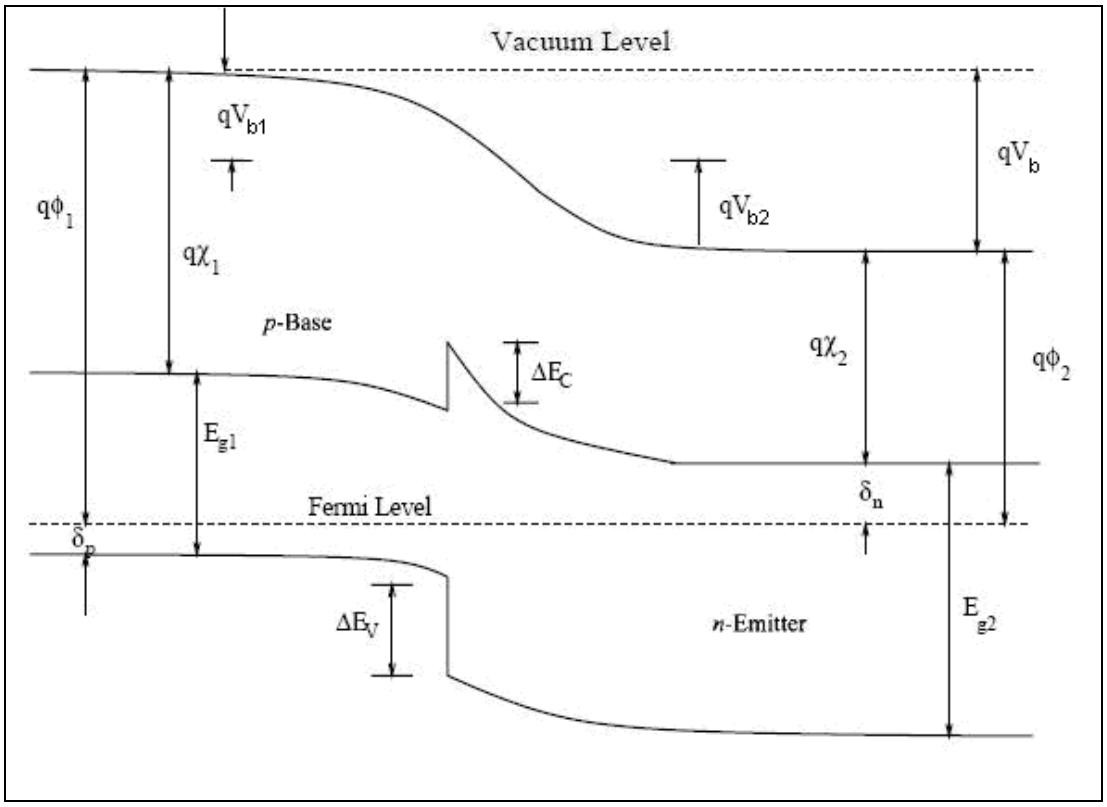

Figure 2.3 : Energy band diagram of a wide band gap n-type semiconductor and a narrow band gap p-type semiconductor in thermal equilibrium [25].

2.2 Material Properties

Polycrystalline thin-film chalcopyrite $CuIn_{1-x}Ga_xSe_2$ (CIGS) is one of the appropriate material for high-efficiency photovoltaic (PV) devices because of its high-absorption coefficient and desirable band gap for solar cells. The record

laboratory efficiency of polycrystalline thin-film solar cells based on CIGS has exceeded 19.3 % [9], while single-crystal based CIGS solar cells have just reached 13 % [28]. Thin film material has many advantages. They can be formed on cheap soda-lime glass and can be prepared by various methods. A wide variety of techniques have been used to deposit CIGS thin films. CIGS based solar cells have shown efficiencies with no evidence of reduction of the absorber layer with time or light exposure. They showed excellent radiation hardness under irradiation [29]. The CIGS devices have structural tolerance to impurities, defects, and large off stoichiometry, which is manifested by the presence of a series of compounds with different Cu:(In+Ga):Se ratios such as 1:1:2, 1:3:5, 1:5:8, etc [30]. In addition, CIGS has a direct band gap and a high absorption coefficient. The band gap of $CuInSe_2$ (x=0) (CIS) and $CuGaSe_2$ (x=1) (CGS) is about 1 eV and 1.7 eV, respectively. Hence, the band gap of CIGS can be varied between 1 eV and 1.7 eV by the addition of gallium [31]. In other words band gap depends strongly on the Ga/In+Ga ratio. The band gap equation of $CuIn_{1-x}Ga_xSe_2$ stoichiometric composition is given by [32]

$$\mathbf{E_g=1.011+0.664x-0.249(1-x)} \quad . \qquad (2.4)$$

For Cu-poor film is given by

$$\mathbf{Eg= 1.0032+0.71369x} \quad . \qquad (2.5)$$

These equations are described in Figure 2.4. The band gap of $CuIn_{1-x}Ga_xSe_2$ films varies with changing the Ga content of the films over the range of composition.

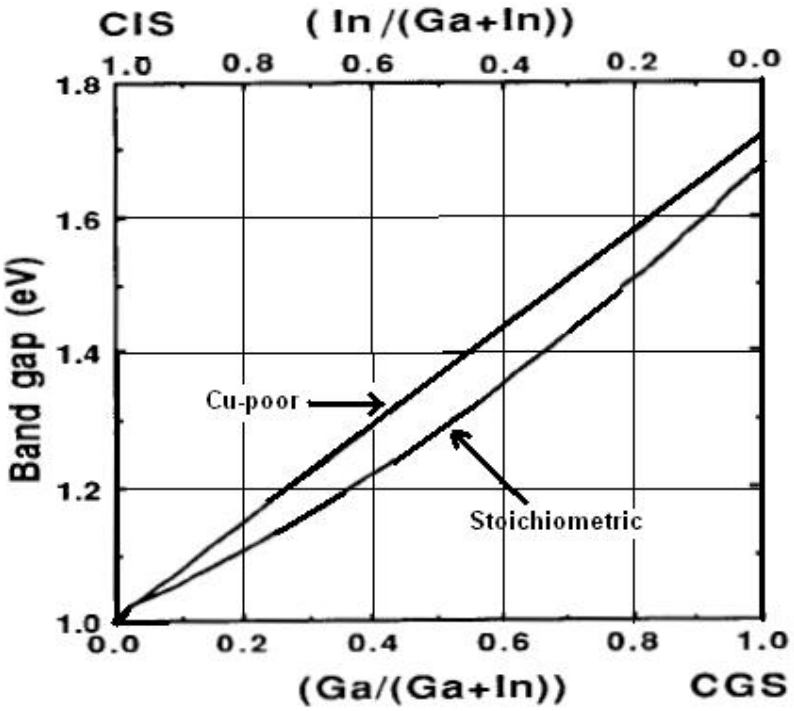

Figure 2.4 : Change in band gap value as a function of Ga/InGa ratio [32].

2.2.1 Crystal Structure of $CuIn_xGa_{1-x}Se_2$ (CIGS)

In ternary ABX_2 semiconductors, $CuIn_{1-x}Ga_xSe_2$ belongs to ternary chalcopyrite $A^IB^{III}X_2^{VI}$ compounds which are an isoelectronic analogue of the binary II-VI zinc-blende compound. Here A=Cu,Ag ; B= Al,In,Ga,Tl ; X=S,Se,Te. The crystal structure of the ternary chalcopyrite relates to nansymmorphic space group D_{2d} , which is a superlatice of zinc-blende structure Td [33]. The chalcopyrite ABX_2 unit cell crystal structure is shown in Figure 2.5. Three distinct structural differences compared with zinc-blende structure are exist. First, two cation sublattice are exist rather than one. Second , the unit cell is tetragonally deformed with a distortion parameter $\eta \equiv c/2a \neq 1$ which causes crystal-field

splitting. The crystal-field splitting and tetragonal distortion are dependent on *x*. For CIGS with $x < 0.1$, $c > 1$ and $\Delta_{cf} > 0$, whereas $x > 0.1$, $\eta < 1$ and $\Delta_{cf} < 0$ [34].

The crystal field parameter Δ_{cf} is defined by

$$\Delta_{cf} = \frac{3}{2} b \left(2 - \frac{c}{a} \right) . \tag{2.6}$$

where b is the negative deformation potential. Third, the anions are displaced from the ideal tetrahedral site by an amount u. The two near-neighbor bond distances are

$$R_{AX} = a\left[u^2 + \left(1 + \eta^2\right)/16 \right]^{1/2} \tag{2.7}$$

and

$$R_{BX} = a\left[(u - \frac{1}{2})^2 + \left(1 + \eta^2\right)/16 \right]^{1/2} . \tag{2.8}$$

where a is the cubic lattice constant. The bond length mismatch is

$$\alpha = R_{BX}^2 - R_{AX}^2 = (u - \frac{1}{4}) a^2 \tag{2.9}$$

where $u \equiv \frac{1}{4}$ and disappears for a zinc-blende like undistorted anion sublattice[35].

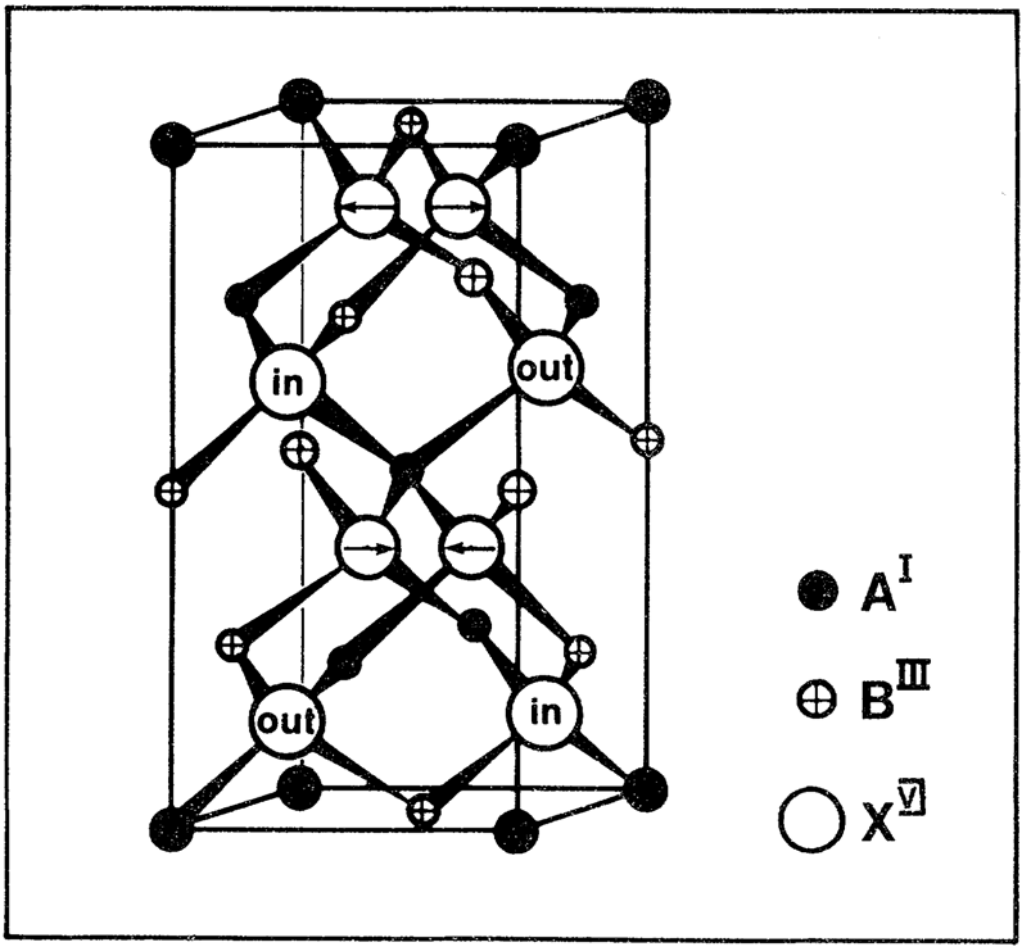

Figure 2.5 : The chalcopyrite ABX_2 unit cell crystal structure. The arrow and the denoted in and out of plane directions show the anion displacements relative to tetrahedral structure [33].

2.3 Structural Characterization

Several techniques have been used to characterize material properties. X-ray Diffraction (XRD) is used to investigate the crystal structure and orientation of the films. Scanning Electron Microscope (SEM) revealed that the grain/particle size and

other microscopic properties of the samples. Energy Dispersive Spectrum (EDS) integrated in SEM system is used for composition analysis. The surface morphology of samples is investigated by Atomic Force Microscopy (AFM). Energy Dispersive X-ray Analysis (EDXA) is used to analyze the composition of the samples.

2.3.1 X-ray Diffraction (XRD)

X-ray diffraction (XRD), as a non-destructive technique, is an important tool for the structural investigation of crystalline materials. It is utilized to study information on structure, phase, lattice parameter and crystal orientation of the thin film samples. X-ray beam which is Cu-Kα and λ= 1.54059 Å scatters from each set of lattice planes (hkl) at specific angles. The peak intensity of a given reflection is proportional to the number of (hkl) planes in the reflecting condition.The diffracting planes (hkl) angles (the incident beams and diffracted beams) are equal. The principle of process is based on Bragg's law, shown in Figure 2.6.

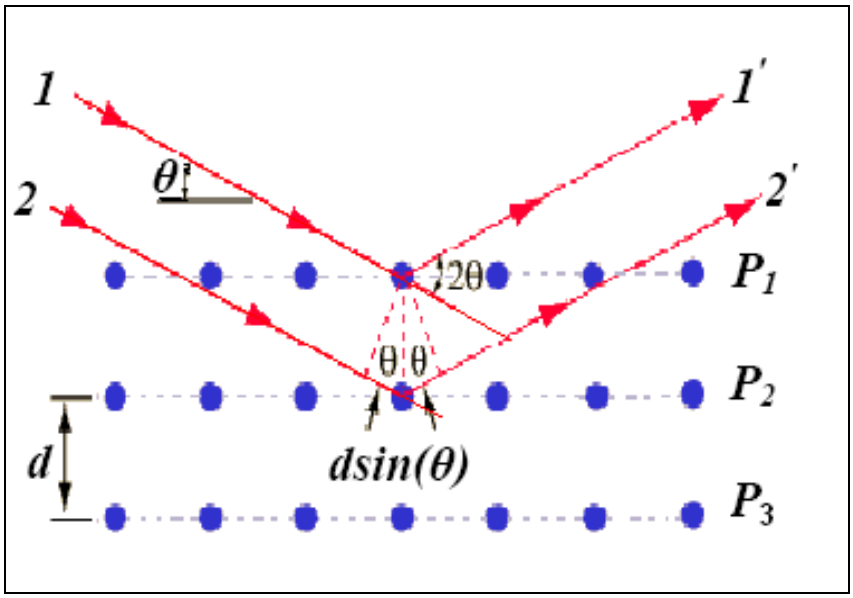

Figure 2.6: X-Ray Diffraction (XRD) atomic planes diagram [35].

An X-Ray beam incident with angle θ and wavelength λ comes on parallel lattice planes P_1 and P_2. Diffraction happens only at the condition of two waves 1' and 2'. The difference between 1 and 1' must be equal to 2 and 2' with an integral number of wavelengths represented by n. This case is known as Bragg's law [35]

$$2d\sin\theta = n\lambda \quad \text{or} \quad d = \frac{n\lambda}{2\sin\theta} \tag{2.10}$$

where d is the interatomic distance and λ is the X-Ray wavelength. We cannot use the visible light due to only for $\lambda \leq 2d$ Bragg scattering can occur.

The lattice parameter d for a cubic structure is given by

$$d_{hkl} = \frac{a}{\sqrt{h^2 + k^2 + l^2}} \tag{2.11}$$

and for a tetragonal structure the lattice parameter is given by

$$d_{hkl} = \frac{a}{\sqrt{h^2 + k^2 + l^2\left(\frac{a^2}{c^2}\right)}} \qquad (2.11)$$

where (hkl) describes the crystal orientation and a and c are lattice constants.

Peaks of every polycrystalline material is unique and each peak is related to specific atomic plane diffraction. This property can be used to identify polycrystalline materials.

In our experiment, Rigaku Miniflex system with CuK_α radiation and λ= 1.54059 Å in the scan range of $2\theta = 10^o$-80^o with 2^o min^{-1} scan speed was used. The XRD peaks were analyzed with ICDD database (the International Centre for Diffraction Data).

2.3.2 Energy Dispersive X-Ray Analysis (EDXA)

Energy Dispersive X-ray Analysis (EDXA) is a tool used to determine the elemental composition of a samples. This technique is used in conjunction with scanning electron microscopy (SEM).

The designing of electrons around the nucleus of an atom is according to accepted norms considered as a sequence of 'electron shells', labeled K, L, M, N, O, P, and Q from innermost to outermost respectively. Primary electrons of a higher potential energy are needed to displace K-shell electrons than are needed to displace L-shell electrons due to the different binding energy levels of the electrons around the nucleus. Beam of high energy electrons is directed at a sample during EDXA analysis. The bombarding electrons are able to 'knock' shell electrons out of their orbits. These electrons can be replaced by electrons from shells further out. As a

result of this, there are a number of reactions that occur, only the following points are considered due to the purposes of explaining the generation of X-rays. The knocking out of an inner shell electron causes the atom to take on an *induced*, high energy state up to the time which the missing electron is replaced and the atom *relaxes*. Hence there is a difference in energy states. If the difference is large, the extra energy can be released in the form of an X-Ray, which transports energy difference and characteristic of the atomic species wavelength.

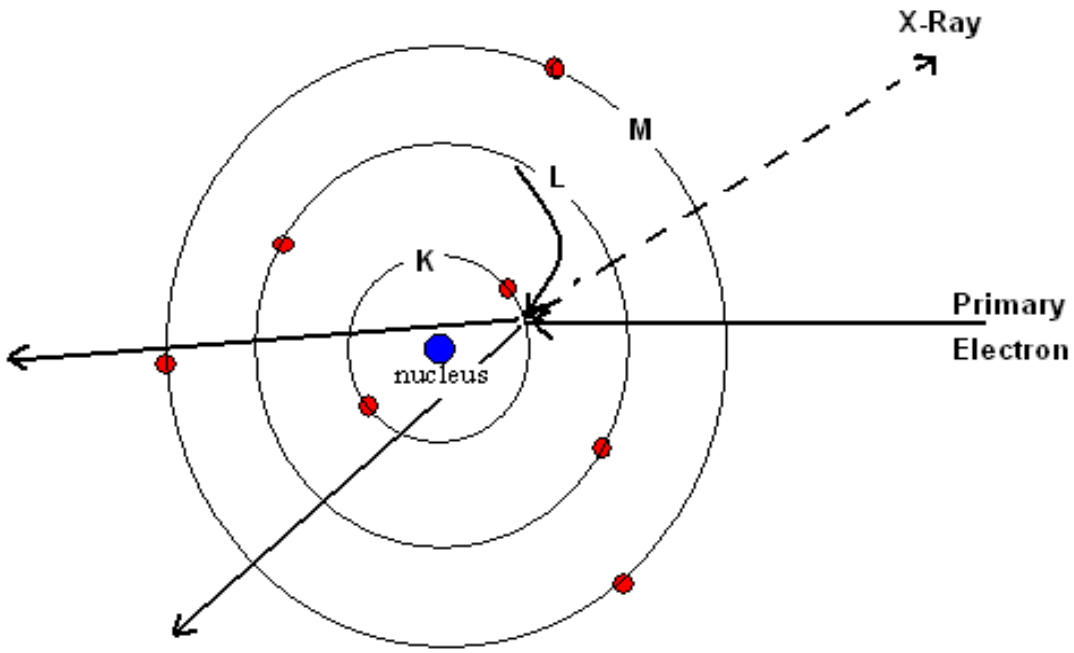

Figure 2.7 : The illustration diagram of Energy Dispersive X-ray Analysis (EDXA).

In our experiment, JSM 6400 scanning electron microscope equipped with EDAX was used in the METU Central Laboratory.

2.4 Electrical Characterization

Electrical characterization technique to determine important parameters for instance type and mobility of carriers, interface quality, oxide trap density, semiconductor bulk defect density, contact and other parasitic resistances are very important aspects of estimating the material quality and device behavior. Electrical characterization contains plenty of technique and measurement but it generally includes resistivity and Hall effect measurement. Important parameters and properties of material such as electrical conductivity, the energy band gap, the majority carriers, deep impurity level, mobility of electrons and holes, device parameters like barrier height, contact resistance, interface densities can be found from these two measurements [36].

2.4.1 Resistivity

Resistivity is one of the most important electrical parameter of the semiconductors. Electrons and holes contribute to the current and determine the resistivity (and also conductivity) in semiconductors. The resistivity is given by

$$\rho = \frac{V}{I}\frac{wt}{L} \tag{2.13}$$

where w is the width of film, t is thickness and L is the spacing between the contacts across the voltage is measured. Conductivity of material can also be found from resistivity. Relation between conductivity and resistivity is expressed by the following relation

$$\rho = \frac{1}{\sigma} \ . \tag{2.14}$$

The electrical conductivity of the thin films is given by

$$\sigma = ne\mu_e + pe\mu_p \tag{2.15}$$

here n and p are concentrations of electrons and holes respectively and μ is the mobility defined as electron drift in semiconductor. The mobility is expressed as

$$\mu_n = -\frac{\langle V_x \rangle}{\langle E_x \rangle} \qquad \left(cm^2 / V.s\right) \tag{2.16}$$

where V_x is carriers drift velocity and E_x is the electric field in the x-direction. In the intrinsic semiconductor, electron and hole concentrations are equal (n=p) and given by

$$n = p = (const.)xT^{3/2} \exp\left[-\frac{E_g}{2kT}\right] . \tag{2.17}$$

Hence, the conductivity can be written as

$$\sigma = (const.)xT^{3/2} \exp\left(-\frac{E_g}{2kT}\right) = \sigma_o \exp\left(-\frac{E_g}{2kT}\right) . \tag{2.18}$$

For an intrinsic semiconductor, the energy band gap can be found from the slope at $ln\sigma$ vs T^{-1} graph.

2.4.2 Hall Effect

The Hall effect was discovered by Edwin Hall in 1879 before electron was not experimentally discovered [37]. After quantum mechanics came into apperance Hall effect had clearly been understood.

The Hall effect method is an important technique which is used to determine experimentally the carrier concentration, carrier type and the mobility in a semiconductor material. When a current-carrying material is placed into an external magnetic field, a voltage will be produced perpendicular to both the current and the field. This principle is known as the Hall effect. The basic foundation of the Hall effect is the Lorentz force law, which is [38]

$$\vec{F} = q\left(\vec{v} \times \vec{B}\right) + q\vec{E} \quad . \tag{2.19}$$

If an electric current flows through a conductor or semiconductor in an external magnetic field, the magnetic field emits a transverse force on the moving charge carriers and it tends to push them to one side of the material. An accumulation of charge at the sides of the material will balance this magnetic force and produce a measurable voltage between the two sides of the material. This measurable transverse voltage is called the Hall voltage or Hall effect. Figure 2.8 shows schematic diagram of the Hall effect. The current applied in the x-direction and magnetic field applied in the z-direction. The Hall voltage is measured along the x-direction. The applied current is given by

$$I = qwtp\upsilon_x \tag{2.20}$$

here *w, t, p* and υ_x are the width, thickness, hole concentration and the drift velocity of carriers of p-type semiconductor material, respectively. The Hall voltage measured along the x-direction is expressed as

$$V_p = \frac{\rho s I}{wt} \tag{2.21}$$

where ρ is the resistivity and *s* is the distance between two contacts. We can derive resistivity from equation 2.21

$$\rho = \frac{V_p}{I}\frac{wt}{s} \quad . \tag{2.22}$$

When the electrons move along negative x-direction, contrary the holes move along positive x-direction. The magnetic field is applied in the z direction. Therefore force is formed in the y-direction. $F=F_y$, $B=B_z$ and $\upsilon=\upsilon_x$. From equation 2.19,

$$E_y = -B_z v_x = \frac{-B_z I}{qwtp} \quad . \tag{2.23}$$

This electric field (E_y) is called the Hall field. It produces a Hall voltage (V_H) along the y-direction and is expressed as

$$V_H = \frac{B_z I}{qtp} \tag{2.24}$$

and the Hall coefficient is defined as

$$R_H = \frac{tV_H}{B_z I} \quad . \tag{2.25}$$

Eventual, the hole density becomes,

$$p = \frac{1}{qR_H} \quad . \tag{2.26}$$

Similarly, the electron density is,

$$n = -\frac{1}{qR_H} \quad . \tag{2.27}$$

As a result using the relation $\sigma = nq\mu$, the Hall mobility is expressed as

$$\mu_H = \sigma R_H \quad . \tag{2.28}$$

Semiconductor's carrier density and type (n-type or p-type) can be determined from direct measurement of Hall voltage.

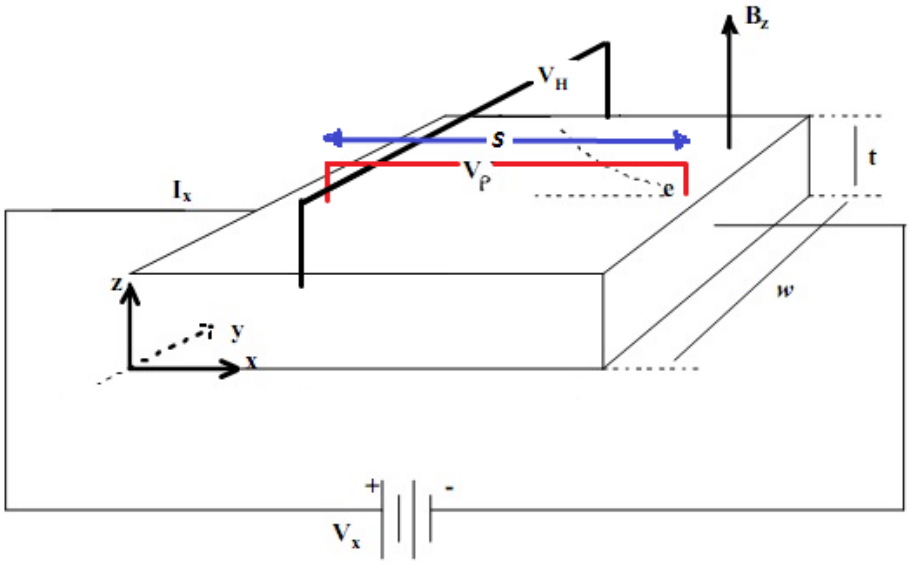

Figure 2.8 : Schematic diagram of Hall effect.

2.5 Optical Characterization

The optical properties of thin films are very important for many applications such as solar power engineering, optoelectronics, integrated optics, microelectronics, and optical sensor technology. Investigation of optical properties of materials

generally focuses on photoconductivity, optical band gap and refraction index and absorption.

2.5.1 Photoconductivity

The effect of light on flow of current through certain solids was observed by Gudden and Pohl in the 1920's [39]. Photoconductivity refers to increase in the electrical conductivity of materials with illumination. It is an optical and electrical phenomenon and associated with carrier excitation, radiative and non-radiative recombination, trapping and various transport mechanisms of extended state conduction.

The carrier density and mobility of material may change under radiation. Dark conductivity of an n-type material is given by

$$\sigma = ne\mu_n \tag{2.29}$$

and increases with illumination. The change of conductivity is expressed as

$$\sigma + \Delta\sigma = q(n_o + \Delta n)(\mu_o + \Delta\mu_o) \tag{2.30}$$

where n_o and μ_o are initial carrier density and mobility respectively; Δn is the change in carrier density and $\Delta\mu$ is the change in carrier mobility. The change in carrier density is generally given by

$$\Delta n = G\tau_n \tag{2.31}$$

here G and τ_n are the photoexcitation and the free electron lifetime respectively. Therefore, the change in conductivity due to illumination is written as

$$\Delta\sigma = e\Delta\mu n + eG\tau_n\mu_o \quad . \tag{2.32}$$

There are several mechanisms which may change the carrier mobility :

- Density and cross section of charged impurities.
- Carriers may be excited to a band with a different mobility.
- Photo excitation may reduce the width of depletion region and the height of the barriers in crystalline materials.

2.5.2 Absorption

The absorption measurement is one of the significant techniques for the determination of band gap of semiconductor materials. This technique is based on interaction of the photons with the material, which gives rise to transmission or absorption according to the energy of the photons. If the incident photon energy is equal or greater than the band gap energy, $h\nu \geq E_g$, electrons are excited from the valance band to conduction band, as a result of the absorption.

On the other hand, if the incident photon energy is less than the band gap energy, $h\nu < E_g$, absorption does not take place. The absorption coefficient represented by α (cm^{-1}) can be found from the following relation via transmission measurement

$$\alpha = \frac{1}{d}\ln\left(\frac{I_o}{I}\right) = \frac{1}{d}\ln\left(\frac{1}{T}\right) \qquad (2.33)$$

here I is the intensity of transmitted light, and I_o is the incident light, d is thickness of material and T is the transmission.

Mainly two types of optical transition can happen at the band gap edge of the semiconductor materials. The first one is direct transition and the other is indirect transition. In the direct transition event, the energy of photon excites the electron and it moves from valance band to conduction band. In the indirect transition event, the enery of photon is not sufficient for excitation of electron. Photon and momentum are exist and simultaneously absorbed by the electron. The direct and indirect transitions are illustrated in the Fig. 2.9.

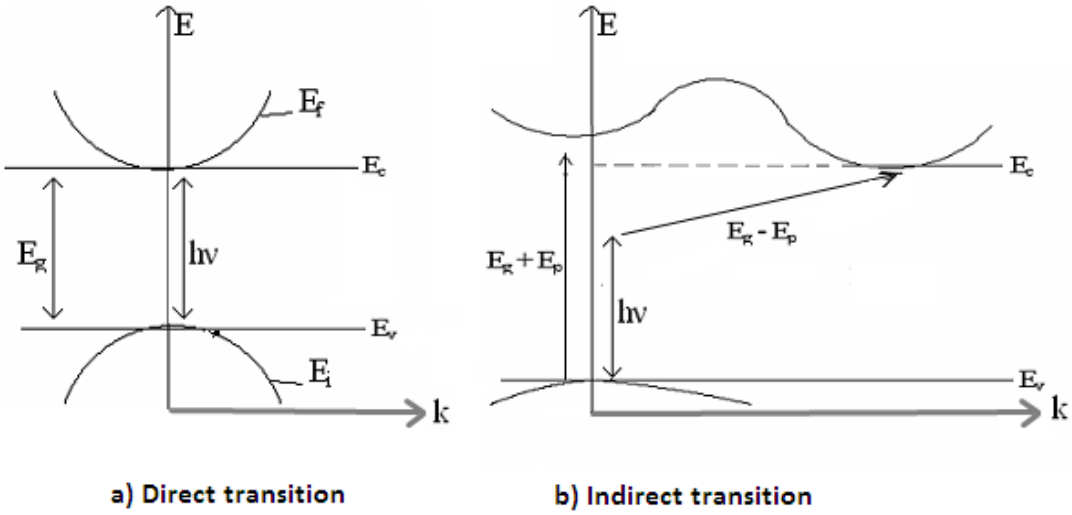

Figure 2.9 : Schematic diagram of a) direct transition and b) indirect transition.

The state energy is given by

$$E = \frac{\hbar^2 k^2}{2m} \tag{2.34}$$

and the electron energy correspond to conduction band is

$$E_e = \frac{\hbar^2 k^2}{2m_e^*} \ . \tag{2.35}$$

In the same way, the hole energy correspond to valance band is

$$E_h = \frac{\hbar^2 k^2}{2m_h^*} \ . \tag{2.36}$$

By using equation 3.35 and 3.36, the transition energy for the direct band gap transition can be defined as

$$h\nu - E_g = E_e + E_h = \frac{\hbar^2 k^2}{2m_e^*} + \frac{\hbar^2 k^2}{2m_h^*} = \frac{\hbar^2 k^2}{2m_r^*} \tag{2.37}$$

where m_r is the reduced effective mass and gived by

$$m_r = \frac{m_e^* m_h^*}{m_e^* + m_h^*} \ . \tag{2.38}$$

The absorption coefficient for direct transition between valance band and conduction band is given as

$$\alpha(h\nu) = A\left(h\nu - E_g\right)^{1/2} \tag{2.39}$$

where A is constant and a function of reduced electron and hole masses.

For indirect transition, the maximum of valance band and minimum of conduction band do not take place at the same wave vector. Therefore, during the excitation of electrons, momentum and energy have to be conserved. These conditions are satisfied by absorption or emission of phonon for indirect band transitions. The absorption coefficient for indirect transition involves phonon absorption and emission and it is written as

$$\alpha_a(h\nu) = \frac{A\left(h\nu - E_g + E_p\right)^2}{\exp\left(E_f \big/ k_B T\right) - 1} \quad \text{for} \quad h\nu > E_g - E_p \tag{2.40}$$

and

$$\alpha_a(h\nu) = \frac{A(h\nu - E_g - E_p)^2}{1 - \exp\left(-E_p / k_B T\right)} \qquad \text{for} \quad h\nu > E_g + E_p \tag{2.41}$$

respectively. According to Bose-Einstein statistics, the term $[exp\ (E_p/k_BT)-1]^{-1}$ gives the number of phonons, and E_p stands for absorbed or emitted phonon energy. Because of absorption and emission processes are possible in the indirect transition, absorption coefficient when $h\nu > E_g + E_p$ must be expressed as

$$\alpha(h\nu) = \alpha_a(h\nu) + \alpha_e(h\nu) \tag{2.42}$$

where α_a and α_e are absorption coefficient standards for phonon absorption and emission, respectively [40].

Impurity effects in the absorption may be observed as well as band to band absorption. These effects contain donor-valance band, acceptor-conduction band and acceptor-donor transitions.

CHAPTER 3

EXPERIMENTAL TECHNIQUES

3.1 Introduction

In this chapter, the details of the $CuIn_{1-x}Ga_xSe_2$ (CIGS) thin film growth and, heat treatment procedures, structural characterization measurement methods, electrical and optical characterization, analysis of experimental data are briefly summarized. Soda lime glass and indium tin oxide (ITO) coated glass slides were used as the substrates for the thin film deposition by the e-beam and thermal evaporation techniques. For the investigation of annealing effect on samples, the deposited films were annealed at different temperatures under the nitrogen atmosphere. The characterization methods were performed both for as-grown and annealed samples. Structural characterizations of the samples were performed by X-Ray diffraction (XRD) and compositional analyses of the samples were determined by Scanning Electron Microscope (SEM) equipped with Energy Dispersive X-ray Analysis (EDXA). The temperature dependent photoconductivity measurements were performed under different illumination intensities in the temperature range of 100-400 K and in the wavelength range of 325-900 nm. The temperature dependent electrical conductivities as a funcion of temperature in the same temperature region were measured to investigate the electrical characteristics of the samples.

3.2 Preparation of CIGS Thin films

The procedures of powder preparation, substrate cleaning and CIGS thin film deposition are briefly explained as follows.

3.2.1 Preparation of Powder, Substrate and Samples

Three different compositions of $CuIn_{1-x}Ga_xSe_2$ (x=0.50, 0.70 and 0.90) have been prepared by direct reaction of high purity elemental copper (Cu), indium (In), gallium (Ga) and selenium (Se).

Stoichiometric amount of the individual elements; copper (Cu), indium (In), gallium (Ga) and selenium (Se) according to the required composition are placed in a quartz ampoule. The ampoule is evacuated to a pressure of $\sim 10^{-6}$ Torr and then sealed. The quartz ampoule with the mixture of elements is placed in a furnace which is heated at rate of 100 ^{o}C per hour (^{o}C/h) in steps up to 1100 ^{o}C and kept at this temperature for 55 hours. The quartz ampoule is then allowed to cool slowly at rate of 100 ^{o}C/h to room temperature. In order to homogenize the molten mixture, during the process of heating and cooling, the ampoule is vibrated constantly.

The glass substrates were first cleaned with a detergent solution to get rid of the gross dirt exist on the surface. Then this process was repeated at about 100 ^{o}C by using an ultrasonic cleaner. The glass slides were then flushed with distilled water. The glass slides were boiled in a solution of 30 % H_2O_2 in order for the organic materials on the surface to gain the water solubility. Finally, the slides were rinsed

with the hot water in the ultrasonic cleaner. The substrates, after the cleaning process, were kept in methanol which were dried by pure nitrogen before deposition.

Two different copper mask geometries for the structural, optical and electrical characterization studies were used to deposit the $CuIn_{1-x}Ga_xSe_2$ (CIGS) thin films. Figure 3.1 a shows the mask shape for structural and optical studies of thin films and Figure 3.1 b shows the van der Pauw (Maltase-Cross) geometry mask to study electrical measurements of the films. Figure 3.2 shows the masks used for metalic contact deposition for van der Pauw geometry. Before deposition, soda lime glass and indium tin oxide coated glass substates should be well cleaned to avoid the formation of impurity between the film and substrate.

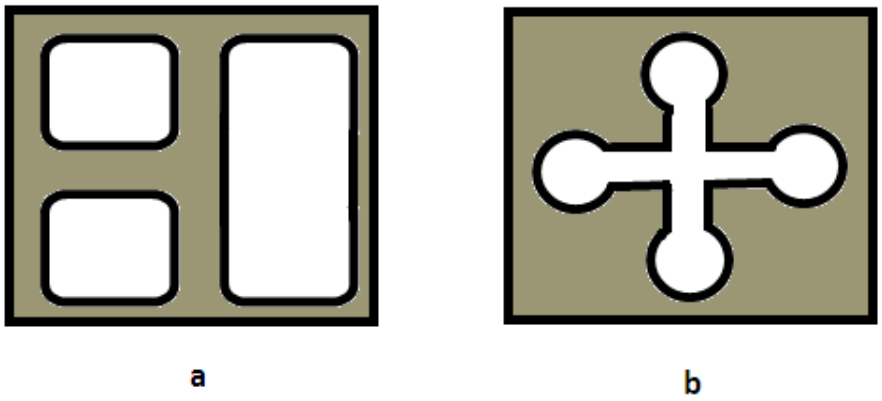

Figure 3.1: The mask geometries for a) structural and optical measurements, and b) electrical measurements of the thin films.

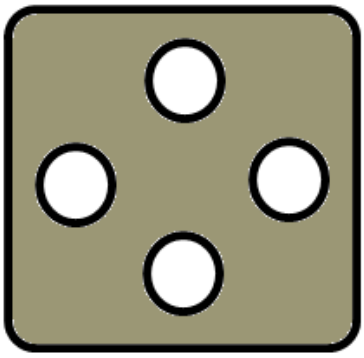

Figure 3.2 : Metal contact geometry for van der Pauw (Maltase-Cross) shape.

3.2.2 Growth Process of CIGS Thin Films

Thin films can be grown on various substrates by applying different techniques such as electron beam evaporation (e-beam evaporation), reactive magnetron sputtering, thermal evaporation, thermal co-evaporation, flash evaporation, pulsed laser deposition (PLD) and physical vapor transport, *etc*.

In this study, electron beam evaporation (e-beam evaporation) and thermal evaporation techniques were used for the growth of CIGS thin films. These two methods and growth conditions are briefly explained as follows.

3.2.2.1 Electron Beam Evaporation

Electron beam (e-beam) evaporation is one of Physical Vapor Deposition (PVD) methods, and the material to be evaporated is in the form of target (powder or ingot). In this study, CIGS powder was placed in graphite crucible and electron beam generated from the gun is accelerated and focused towards the target. Kinetic energy

of the electrons is transformed into thermal energy as bombarding the target. The increasing surface temperature of the target results in the formation of a liquid melt and the material evaporates under vacuum. Then it is condensed on the substrate. This process takes place inside the vacuum chamber which was first evacuated to 10^{-2} Torr by a mechanical pump and then evacuated to ~10^{-6} Torr by a turbo pump. The deposition rate of e-beam evaporation was controlled by using thinkness monitor. The deposition rate can vary from about 1 Angstrom per second to a few nanometers per second.

Figure 3.3 shows the e-beam deposition system. In the e-beam method, the electron beam is created by a filament, and then focused and directed by a permanent magnet set onto the target. Sample holder can accommodate substrates and the thickness of the thin film is observed by a thickness monitor during the deposition.

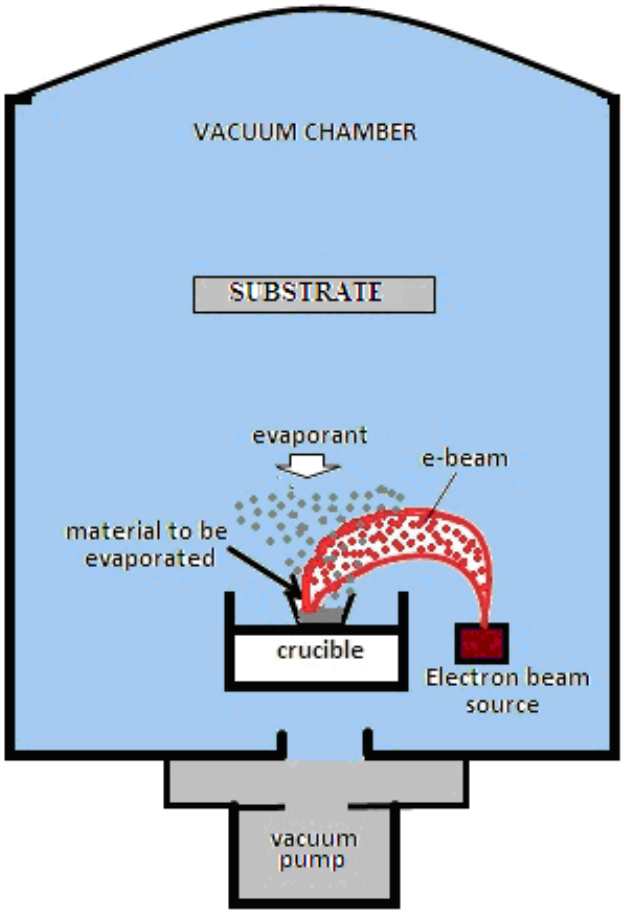

Figure 3.3 : Schematic diagram of electron beam (e-beam) evaporation system.

Figure 3.4 : Picture of electron beam, electron beam source and crucible [41].

With this setup it is possible to deposit the films with different thicknesses. The deposition conditions affect the CIGS thin film morphology which in turn affects the final device performance. The typical deposition conditions of our study with electron beam (e-beam) evaporation method are summarized as :

Source temperature : ~ 800ºC

Substrate temperature: ~ 250^{o}C

Start vacuum : 2x10^{-6} Torr

Final vacuum : 6x10^{-6} Torr

Growth rate : ~ 15 Å/sec

The growth rate can be varied by changing the intensity of electron beam and source temperature. In this study, the thin film thickness vary from 300 nm to 1μm (1000 nm).

3.2.2.2 Thermal Evaporation

The second growth method used is thermal evaporation technique. The thermal evaporation technique is a simple process in which materials are vaporized at a sufficiently high temperature in the vacuum. The vacuum enables vapor particles to travel directly to the substrate. In this method, the thin films were deposited at three stages by using two quartz crucibles (one for evaporation of CIGS powder and the other for evaporation of pure copper (Cu)). The typical deposition conditions of our study with the thermal evaporation method are summarized as :

First source temperature : ~ 750ºC

Second source temperature : ~ 850ºC

Substrate temperature: ~ 250^{o}C

Start vacuum : 4x10^{-6} Torr

Final vacuum : 6x10^{-6} Torr.

Growth rate : 3-6 Å/sec

The thin film thickness vary from 300 nm to 450 nm. The thermal evaporation was applied by using Leybold Univex 300 vacuum system, schematic diagram of which is given in Fig 3.5.

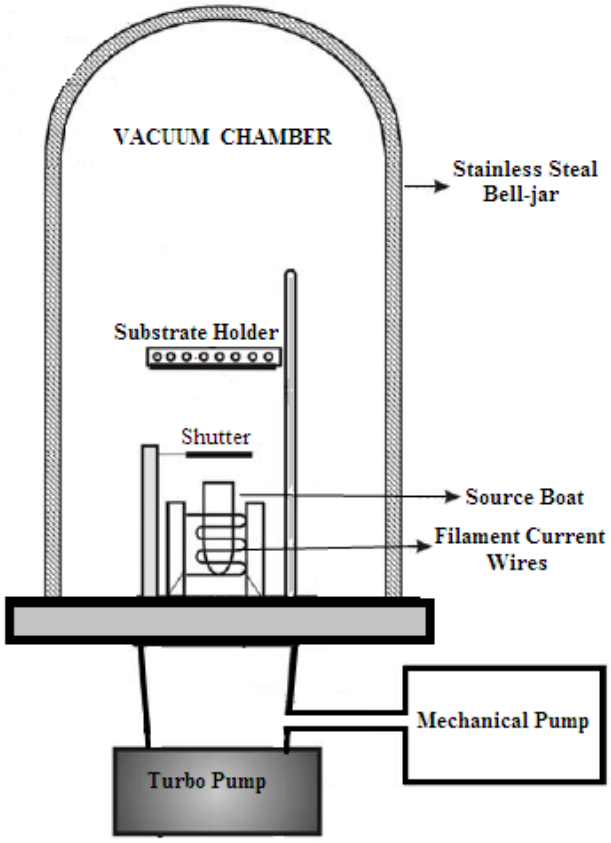

Figure 3.5 : Schematic diagram of the thermal evaporation system.

3.2.3 Annealing

In order to investigate the effect of annealing on the properties of the films, samples were subjected to different annealing procedures. CIGS thin film samples were annealed in nitrojen atmosphere betweeen 300-450 ^{o}C with 15 ^{o}C and 50 ^{o}C steps for 5, 15 and 30 minutes.

3.2.4 Electrical Contacts

Ohmic indium (In) contacts to the CIGS thin films for electrical and optical measurements were applied by metallic evaporation using the masks illustrated in Fig.3.2.

The metallic evaporations were applied by using Nanotech evaporation system as shown in Fig. 3.6. The lowest derivable pressure in this system was 10^{-6} Torr by using an oil diffusion pump with a liquid nitrogen trap. Indium (In) with the purity 99.9995 % was used as the ohmic contact material. It was placed in a molybdenum boat heated by a manually controlled variac. The metallic evaporation process took about 5 minutes allowing a 200-500 Å thin metallic layer on the surface of the CIGS thin film.

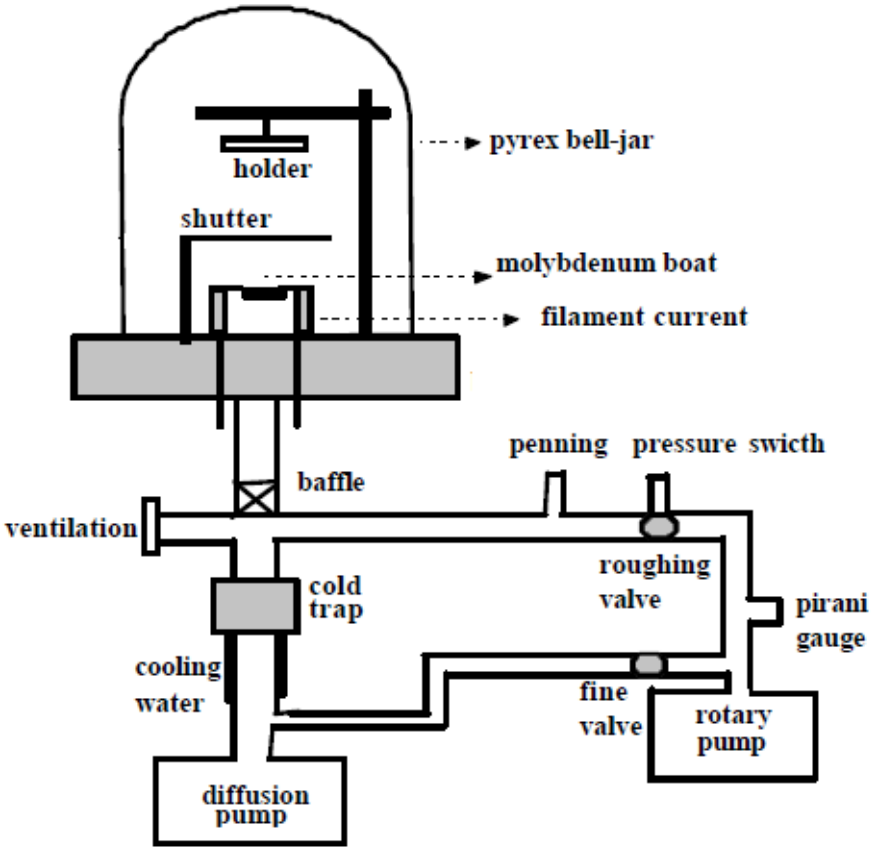

Figure 3.6 : Schematic diagram of metallic evaporation system.

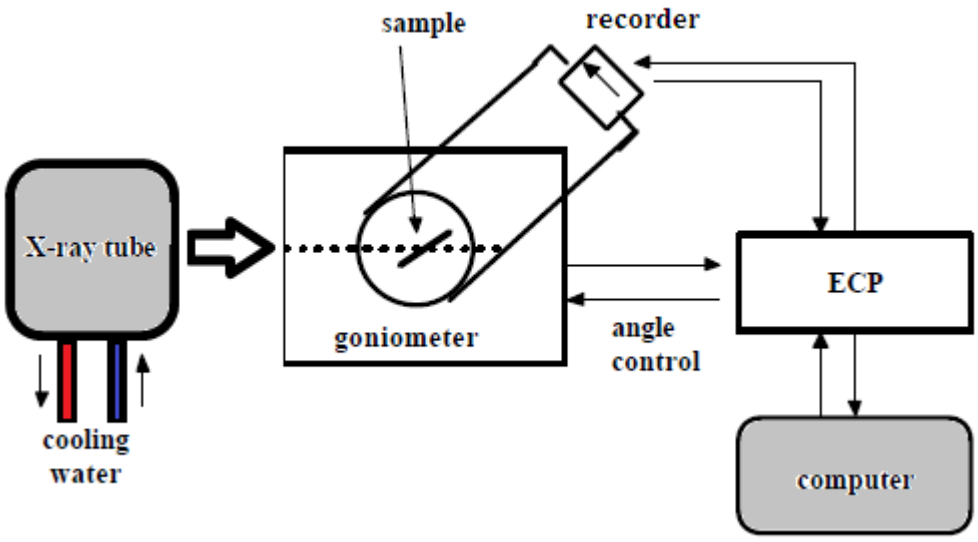

Figure 3.7 : Schematic diagram of X-Ray Diffraction system.

3.3 Structural Measurements

A powder X-Ray Diffractometer with CuKα radiation and Energy Dispersive X-ray Analysis (EDXA) were used to investigate the structural properties of CIGS thin films deposited on the soda lime glass substrates.

3.3.1 X-Ray Diffraction Analysis (XRD)

The phases and the crystallinity of the CIGS thin films were determined by the X-Ray diffraction analysis. X-Ray diffraction measurements were carried out by using a Rigaku Miniflex X-ray diffraction system equipped with Cu-Ka radiation of average wavelength 1.54059 Å in the scan range of $2\theta = 10^{o} - 80^{o}$ with 2 degree/min scan speed. All X-ray diffractograms were taken with the same parameters. The XRD results were examined with a computer software and the International Centre for Diffraction Data (ICDD) database which includes the diffraction patterns of well known structures of $CuIn_{1-x}Ga_xSe_2$ (x=0.5 and x=0.7), $CuInSe_2$ and $CuGaSe_2$. The peak matching process was performed to rely on the relative intensities of peaks and the observed peak positions at specific 2θ values. The shematic diagram of X-Ray Diffraction (XRD) system is shown Fig. 3.7.

3.3.2 Energy Dispersive X-ray Analysis (EDXA)

The surface and elemental compositional charecteristics of CIGS thin films were examined using a JSM 6400 scanning electron microscope (SEM) equipped

with Phoenix Energy Dispersive Analysis X-ray (EDXA) in the Central Laboratory, METU. If an electron beam is scanned from one side to other side of the surface of the material, different interactions happen between the electron beam and the sample. The incident electron beam on the surface of the material causes the emission of secondary electrons collected to form a high-magnification image of the surface that is the secondary emission mode of the SEM. The prepared CIGS powder and CIGS thin films grown by e-beam evaporation and thermal evaporation techniques were analyzed by EDXA.

3.3.3 Thickness Measurement

The thickness of the CIGS thin films were checked by using a DEKTAK 3030ST profilometer which can measure film thickness from ~10 nm up to 131 μm with a 10 to 20 Å resolution. The system consists of a 12.5 μm diameter stylus and a camera for locating the stylus on the region at which the thickness were to be measured. The stylus can be moved electromechanically on the surface of the film. The thin films were deposited onto glass substrates, so that the thicknesses were measured by scanning the stylus over the glass surface up to the edge of the film surface. Thickness measurements were performed for different regions of the films and it was observed that the thickness over the whole surface was almost unchanged.

3.4 Electrical Measurements

The electrical characterization of the CIGS thin films including the temperature dependent dark resistivity and mobility measurements was carried out in the temperature range from 100 K to 400 K via a Janis Liquid Nitrogen VPF Series Cryostat. The temperature of the samples was measured with a GaAlAs diode sensor inside the cryostat and controlled by a LakeShore-331 temperature controller. The vacuum of cryostat was supplied by the Univac Rotary pump. The temperature of the sample was progressively increased by 10 K steps from 100 K to 400 K.

3.4.1 Resistivity Measurements

The reliability of the electrical measurement depends on the ohmic behaviour of the metal contacts. So the current-voltage measurement was performed between any two successive contacts of van der Pauw samples to check the ohmicity of the contacts. The *LogI- LogV* plots were found to be linear with a slope of almost unity and variation is symmetrical with the reversal of the current, indicating the ohmic behaviour of the contacts.

The commonly used method to measure the resistance of thin films is van der Pauw technique which is illustrated in Fig. 3.8. Imperfect alignment and thermoelectric voltage produced by the thermal gradient between probes are eliminated by this method. The current is supplied by the Keithley 220 programmable current source and the voltage is measured by a Keithley 2001 multimeter. In order to reprogram the current source for providing highest possible

current without passing the voltage limit, voltage between the current probes has been measured by Keithley 619 Multimeter. A list of voltages measured for this method is given in Table 3.1.

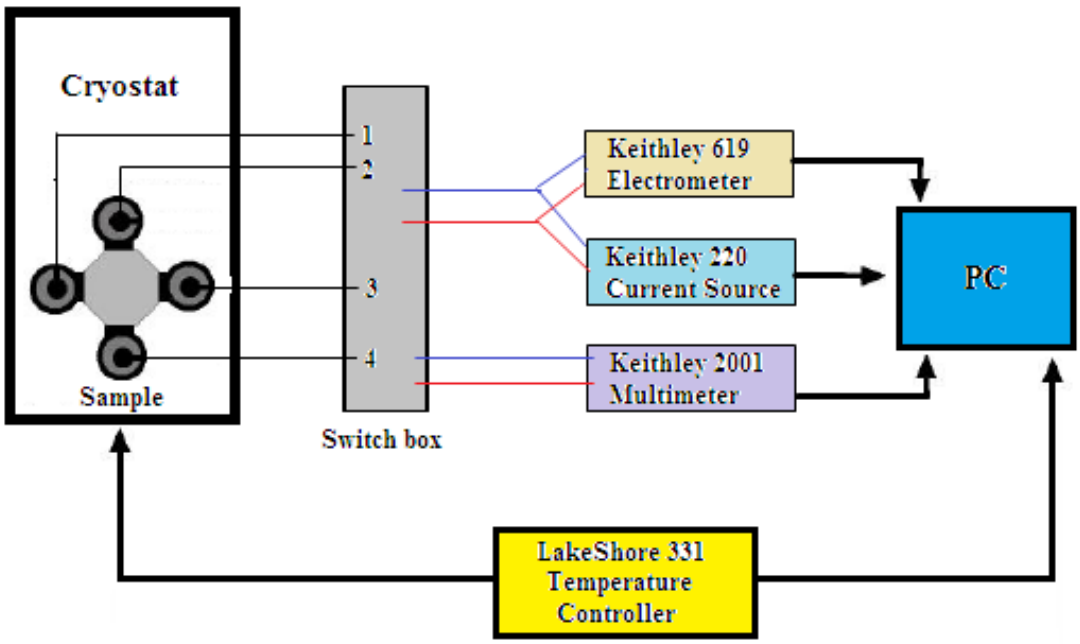

Figure 3.8 : The experimental set-up for the resistivity measurements of van der Pauw type sample.

Table 3.1 The list of measured voltages for van der Pauw method.

Voltage Number	Current Applied Between	Voltage Measured Between
V_1	1-2	3-4
V_2	2-1	3-4
V_3	2-3	1-4
V_4	3-2	1-4
V_5	3-4	1-2
V_6	4-3	1-2
V_7	4-1	2-3
V_8	1-4	2-3

The voltages measured and listed as Table 3.1 and then two resistivity (ρ_A and ρ_B) calculated as follows [42]

$$\rho_A = \frac{\pi}{2\ln 2}\frac{t_s}{I} f_A (V_2 + V_4 - V_1 - V_3) \tag{3.1}$$

$$\rho_B = \frac{\pi}{2\ln 2}\frac{t_s}{I} f_B (V_6 + V_8 - V_5 - V_7) \tag{3.2}$$

where ρ_A , ρ_B are resistivity (ohm-cm), t_s is the thickness (cm), I is the current (amperes), f_A, f_B are geometrical factors on the basis of sample symetry and they equal one ($f_A = f_B = 1$) for perfect symmetry. The average resistivity ρ_{AVG} can be calculated as follows

$$\rho_{AVG} = \frac{\rho_A + \rho_B}{2} \ . \tag{3.3}$$

3.4.2 Hall Effect Measurements

The Hall effect measurements were performed on van der Pauw geometry samples by dc-method because of the high resistivity of samples (10^6-10^9 ohms). The same circuit design as resistivity was used for Hall effect measurements with magnetic field perpendicular to the sample surface and the current. The magnetic field produced by Walker Magnion Model FFD-4D electromagnet. Power of magnetic field was remained constant about 1 Tesla in all measurements. The experimental set up for Hall effect measurements is illustrated in Fig. 3.9.

First, a current was applied between contacts 1 and 3 without a magnetic field, and the potential drop between 2 and 4 was maesured. Then, the resistance $R_x = (V_4 - V_2)/I$ is calculated. Secondly, the same current and magnetic field were applied together, and the potential drop was measured, and then the resistance $R'_x = (V_4 - V_2)/I$ was calculated. The difference between two resistance values with and without magnetic field ($\Delta R_x = R_x - R'_x$) was calculated. In the later step, the current was applied between contacts 2 and 4 with and without magnetic field, and the potential drop was read by Keithley 619 Multimeter. The resistance difference ($\Delta R_y = R_y - R'_y$) was found.

The Hall coefficient R_H was calculated from the two resistances (ΔR_x and ΔR_y) as following

$$R_H = \frac{\Delta R_x + \Delta R_y}{2}\left(\frac{B}{t}\right) \qquad (3.4)$$

where B is magnetic field and t is the thickness. The carrier density for p-type sample was determined by the relation given below

$$p = \frac{1}{eR_H} \quad . \tag{3.5}$$

Finally, the mobility is found by combining the results of conductivity and Hall measurements as follows

$$\mu = \frac{\sigma}{pe} \tag{3.6}$$

where σ is the conductivity, p is the hole concentration, and e is the electron charge.

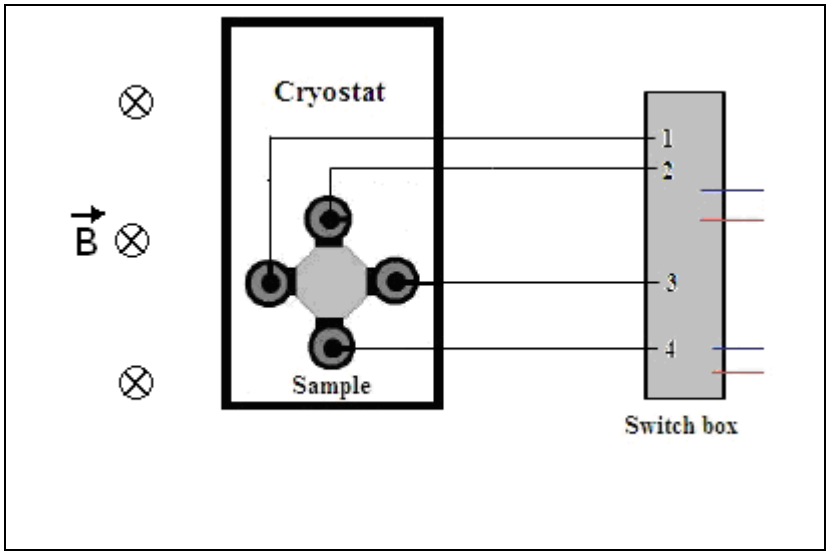

Figure 3.9 : The experimental set-up for the Hall effect measurements of van der Pauw type sample.

3.5 Optical Characterization Measurements

In order to investigate the optical properties of the materials, the photoconductivity and the optical absorption or transmission spectrum measurements have been performed.

3.5.1 Photoconductivity

The photoconductivity measurements were carried out in the Janis Liquid Nitrogen VPF Series Cryostat in the temperature range from 100 K to 400 K. 12-Watt halogen lamp was used as source of illumination and it located at a suitable place above the sample in order to make certain illumination of the whole surface uniformly. The illumination intensity of the halogen lamp was arranged by changing the current from 50 mA to 90 mA with 10 mA steps. For the determination of the illumination intensity values, IL Ford 1700 Radiometer was used. Keithley 220 current source was used as the current provider for the illumination intensity of the halogen lamp. Bias voltages were applied by Keithley 2001 Multimeter and current was measured by the same device. All experiment which related photoconductivity was completely administrated by using LabVIEW computer software program.

3.5.2 Absorption

The transmission measurements have been carried out by Pharmacia LKB Ultrospec III UV-VIS spectrometer in the wavelength region 325-900 nm, and the bare glass substrate has been used in each measurement for reference. All measurements were performed at room temperature (295 K). The optical absorption coefficient was calculated from the measured transmission data. The relation between the absorption coefficient and the incident photon energy was computed from following relation,

$$\alpha h\nu = A\left(h\nu - E_g\right)^n \tag{3.7}$$

where A is a constant, E_g is the band gap energy of semiconductor and n is an index, which changes according to the transition types. For direct transition, n is ½ , and n is 2 for indirect transition [43]. The band gap of material was determined from the extrapolation of $(\alpha hv)^2$ versus hv graph.

CHAPTER 4

RESULTS AND DISCUSSIONS

4.1 Introduction

In this chapter, the results of structural, electrical and optical measurements of the CIGS thin films deposited by two different growth techniques, namely e-beam deposition and thermal evaporation, are presented. Also the effects of annealing temperature and time on the material properties were investigated. The results of the temperature dependence of dark conductivity and Hall effect studies in the temperature range of 100-400 K are discussed. Finally, the optical absorption measurements, the calculation of optical energy gap and the photoconductivity measurements are given.

4.2 Study and Optimization of the Growth Techniques

In this study, nine different runs with different deposition conditions and parameters were performed for the production of $CuIn_{1-x}Ga_xSe_2$ (CIGS) thin films with two different techniques. Electron beam evaporation and thermal evaporation methods were used for the deposition of CIGS thin films from the pre-sintered stoichiometric CIGS powder onto soda lime glass substrates. For all the grown samples X-Ray Diffractometer (XRD) and Energy Dispersive X-ray Analysis (EDXA) were applied to investigate the structural properties and to identify the content of the constituent elements and the phases present in the films. The reason of

doing nine different runs was to optimize the deposition parameters and growth technique to obtain the stoichiometric $CuIn_{0.5}Ga_{0.5}Se_2$ (CIGS) thin film which will be used as absorber layer for thin film solar cells.

The structural and the compositional properties of the CIGS thin film samples obtained by thermal evaporation and e-beam techniques strongly depends on the deposition parameters and the source material. Pure elemental copper (Cu) , indium(In), gallium (Ga) and selenium(Se) with (99,9995 %) pority were used to obtain CIGS single crystal powder as explained in section 3.2.1. The XRD pattern and EDXA result of the powder as seen in Fig. 4.1, Fig. 4.2 and Table 4-1 verified that the powder had polycrystalline $CuIn_{0.5}Ga_{0.5}Se_2$ (CIGS) structure with a preferred orientation along in the (112) direction. The result of EDXA analysis showed that the composition of the CIGS powder was almost stoichiometric.

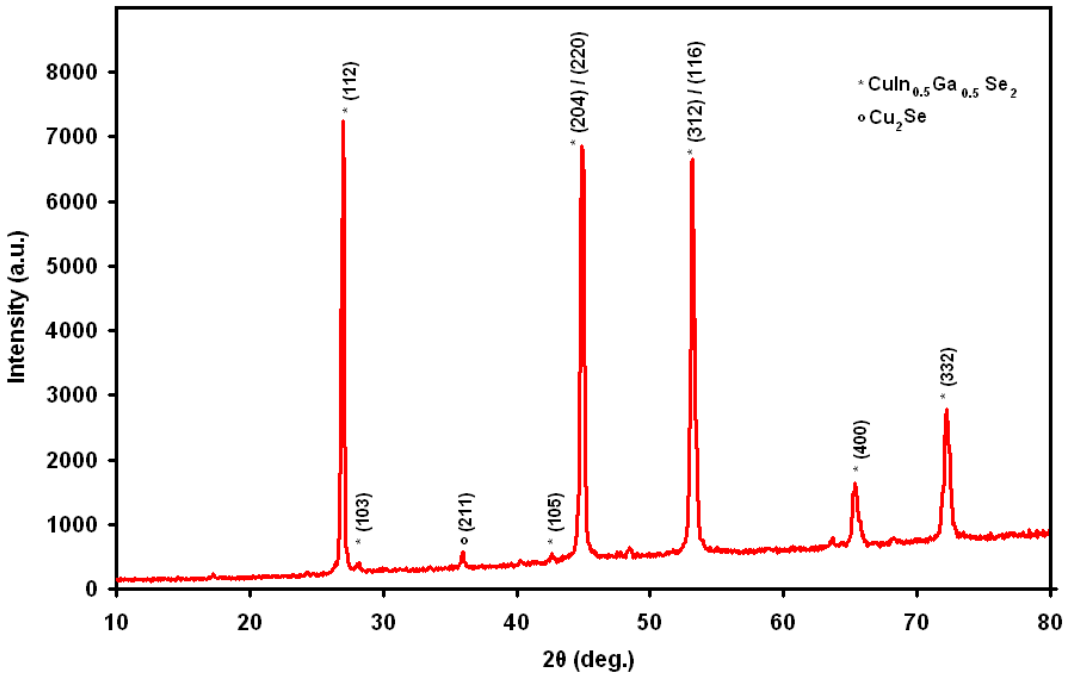

Figure 4.1 : X-ray diffraction pattern of $CuIn_{0.5}Ga_{0.5}Se_2$ powder.

Table 4.1 : EDXA result of $CuIn_{0.5}Ga_{0.5}Se_2$ powder.

	Cu	In	Ga	Se
Powder	**23.91**	**11.86**	**11.99**	**52.23**

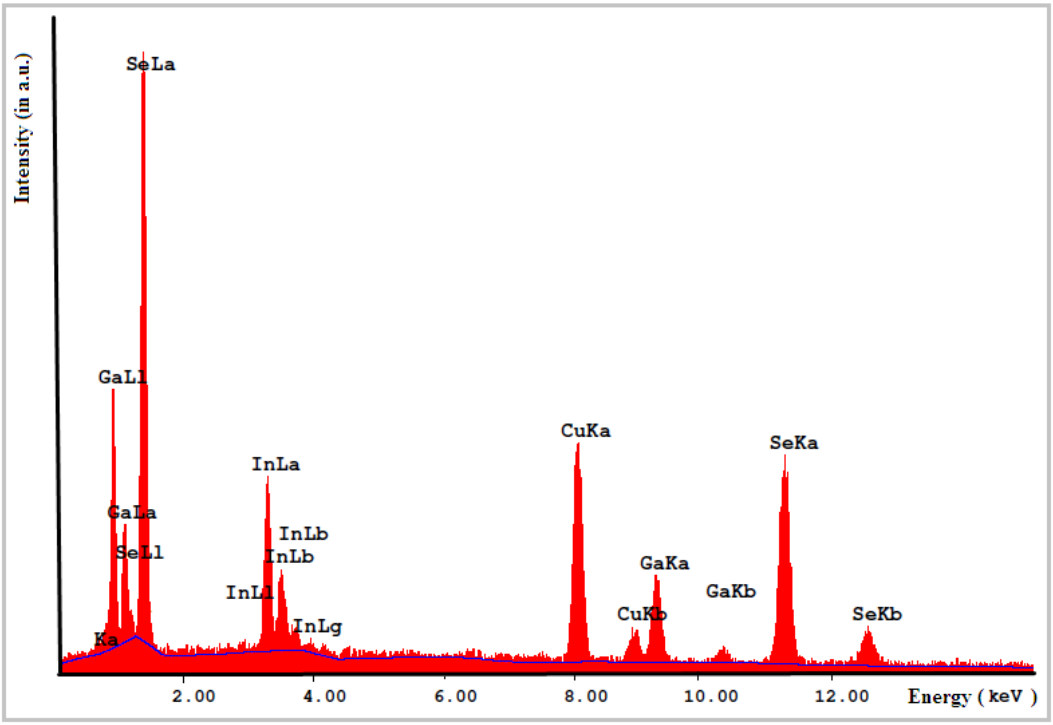

Figure 4.2 : The variation of intensity-dispersive energy obtained from EDXA analysis for $CuIn_{0.5}Ga_{0.5}Se_2$ powder.

In the first growth (namely R1), e-beam evaporation technique was used for production of CIGS thin film. As a result of EDXA, it was observed that samples were copper (Cu) rich and indium (In), gallium (Ga) and selenium (Se) deficient as tabulated in Table 4.2. It was observed that the copper concentration increased after annealing the samples at 450 ^{o}C for 30 minutes (Ann 450 ^{o}C).

Table 4.2: EDXA results of first growth (R1).

CIGS Films	Cu	In	Ga	Se
As grown	66.76	0.55	0.45	32.25
Ann 450 ^{o}C	81.33	1.03	1.26	16.37

In the second e-beam evaporation run (R2), CIGS thin films were obtained by reducing the beam intensity and growth rate to decrease the Cu concentration. The deposited films were annealed at 300, 350, 400 and 450 ^{o}C for 30 minutes to increase the crystalinity. The XRD results of the as grown and annealed films were shown in Fig. 4.3. The intensity of peak corresponding to $CuInSe_2$ phase increases with the increasing annealing temperature since CIGS structure could not be obtained as a result of this run either. As the following run, thermal evaporation method was used.

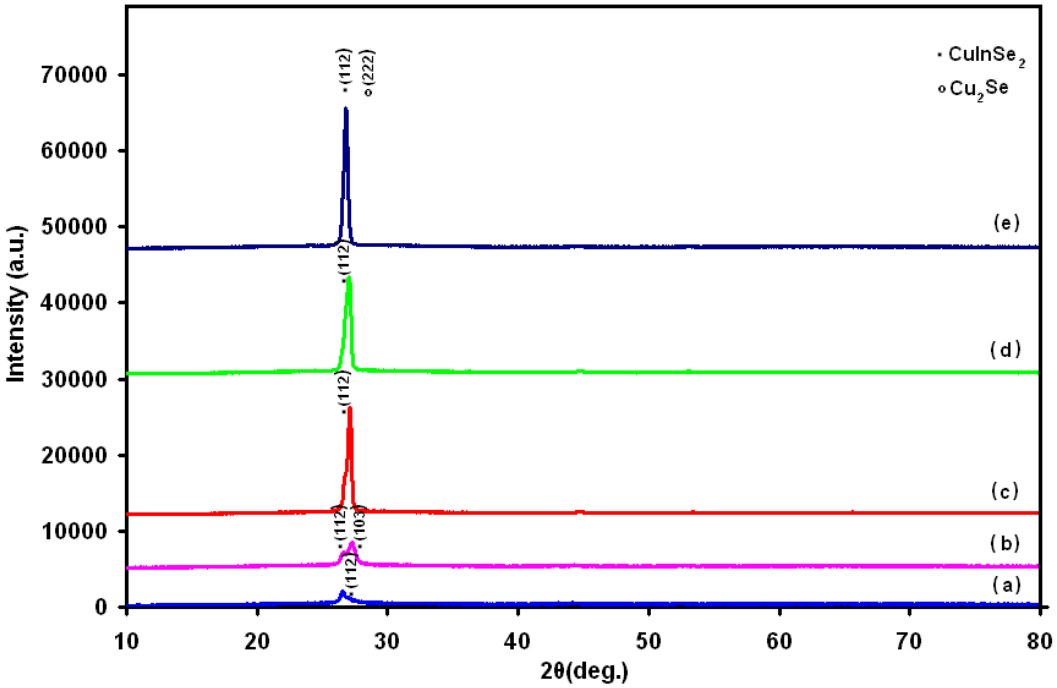

Figure 4.3: X-ray diffraction patterns for the samples deposited by e-beam technique (R2) (a) as grown and annealed at (b) 300 ^{o}C, (c) 350 ^{o}C, (d) 400 ^{o}C, (e) 450 ^{o}C.

In the first thermal evaporation run (RT1), CIGS thin films were deposited thermally from CIGS powder in a quartz crucible by using Leybold Univex 300 vacuum system. All growth parameters were the same with the previous runs. The XRD results of as grown and the annealed samples which were illustrated in Fig. 4.4, showed that the samples had multiphase structure with the phases of Cu_2Se, $CuInSe_2$ and $CuGaSe_2$. The films with the amorphous structure in the as grown forms became polycrystalline after being annealed at 350 ^oC.

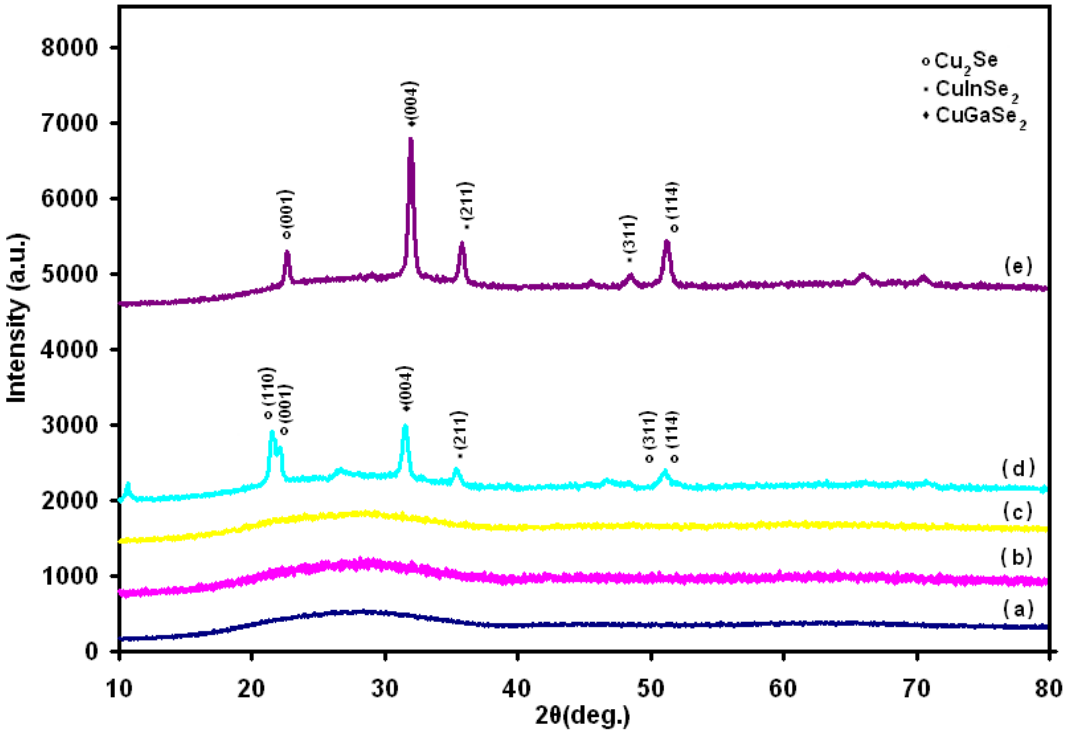

Figure 4.4 : X-ray diffraction patterns for the samples deposited by thermal evaporation method (RT1) (a) as grown and annealed at (b) 250 ^oC, (c) 300 ^oC, (d) 350 ^oC, (e) 450 ^oC.

In order to overcome the deficiency of Cu in the structure the second thermal evaporation run (RT2) was carried out by using a second source for copper to deposite excess copper layer. Double sources were used sequentially for the thermal evaporation. First 150 nm CIGS thin film, subsequently, 100 nm Cu and again 150 nm CIGS were deposited layer by layer.

Following the growth, XRD scan was carried out. The analysis showed that the diffraction peaks were related to $CuInSe_2$ not to CIGS structure (Fig.4.5)

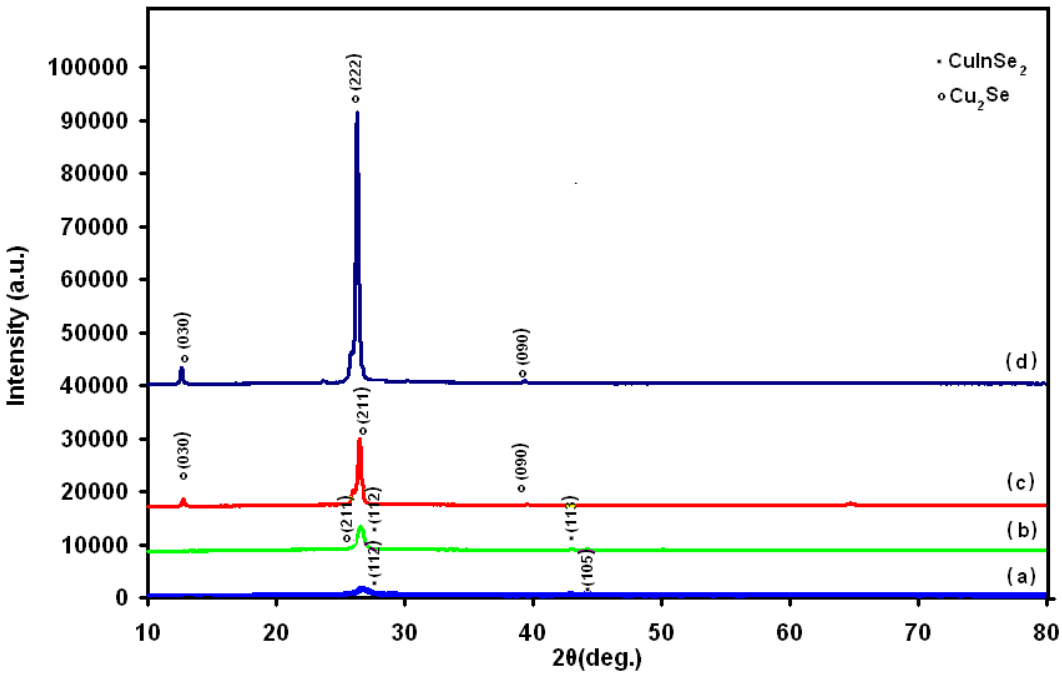

Figure 4.5 : X-ray diffraction patterns for the samples deposited by thermal evaporation method (RT2) (a) as grown and annealed at (b) 300 ^{o}C, (c) 350 ^{o}C, (d) 400 ^{o}C.

The studies on the samples obtained by thermal evaporation indicated that controlling the structure of the thin film material by this technique is very difficult. So in the following runs e-beam evaporation technique was used to obtain the appropriate single phase CIGS polycrystalline thin film material. Several different runs were performed with different growth rates and/or introducing excess selenium into the source powder and evaporating excess Se and Cu layer from second source. After repeating layer by layer deposition by the e-beam method single phase CIGS films were obtained with the procedure described below as the last run (RL).

In the last e-beam evaporation run (RL), the CIGS thin films were deposited at three stages by using two sources; one for evaporation of CIGS powder and the other source for e-beam evaporation of pure Cu. The CIGS-Cu-CIGS layers were then subsequently deposited onto soda lime glass. As the result of this process, stoichiometric $CuIn_{0.5}Ga_{0.5}Se_2$ (CIGS) thin films were obtained. For the rest of the chapter, the discussions of the characterization results for these samples were presented.

4.3 Structural and Compositional Characterization

Using the prepared polycrystalline stoichiometric $CuIn_{0.5}Ga_{0.5}Se_2$ (CIGS) powder material, CIGS thin films were deposited onto soda lime glass substrates by the described e-beam technique. The thickness of the samples changes from 350 nm to 700 nm.

4.3.1 X-ray Diffraction Results

The structure and composition of the films were measured by means of X-ray difraction and the energy dispersive X-ray analysis (EDXA) performed with the SEM measurements. In the following sections the results of these studies are presented.

For the identification of the structure and the phases present in the deposited films, XRD studies were performed for the samples which were subjected to three different annealing procedures (samples S1, S2 and S3). First group of as grown samples was annealed at 350, 400 and 450 ^{o}C under the nitrogen atmosphere for 30 minutes (S1) and XRD measurements were carried out after each annealing steps. The typical XRD patterns for the as grown and the annealed films are given in Fig. 4.6 and Fig. 4.7 respectively.

The XRD diffractograms illustrated in Fig. 4.6 show that the as grown CIGS thin films deposited at the substrate temperature of 300 ^{o}C have a polycrystalline structure. The samples also exhibit polycrystalline structures after annealing at the indicated temperatures and time (Fig. 4.6). When the XRD diffractograms of the CIGS thin films were compared with the ICDD database, the peaks were indexed as in the ICDD Card No. 40-1488 and the preferred directions were found to be along (112), (103), (105) and (204)/(220) direction for as-grown and annealed CIGS thin film samples. According to ICDD reference card, the CIGS thin films have tetragonal crystal structure with lattice parameters of a: 5.69, c: 11.32 Å. Contreras et al. [44] and Dhere et al. [45] has reported similar results for the CIGS thin films.

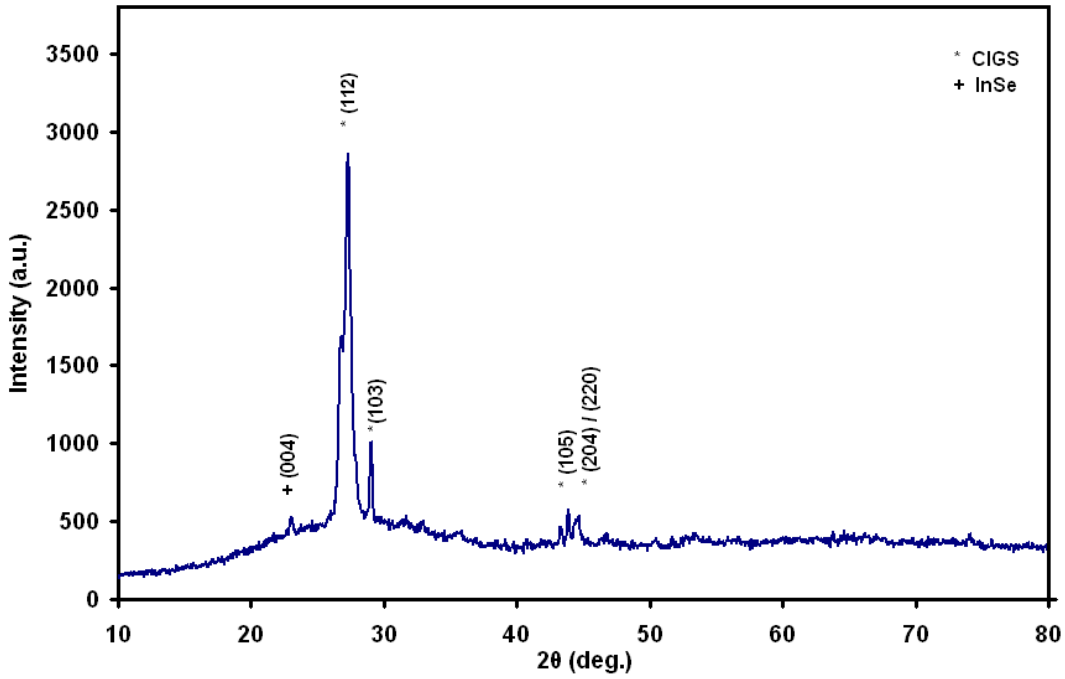

Figure 4.6 : X-ray diffraction pattern for as-grown CIGS thin film.

Intensities of the peaks were observed to increase with the increasing annealing temperature at the same positions with the emerging (312)/(116) peak of CIGS at 450 ^{o}C. The (004) peak of InSe indicates the existance of InSe in the CIGS structure.

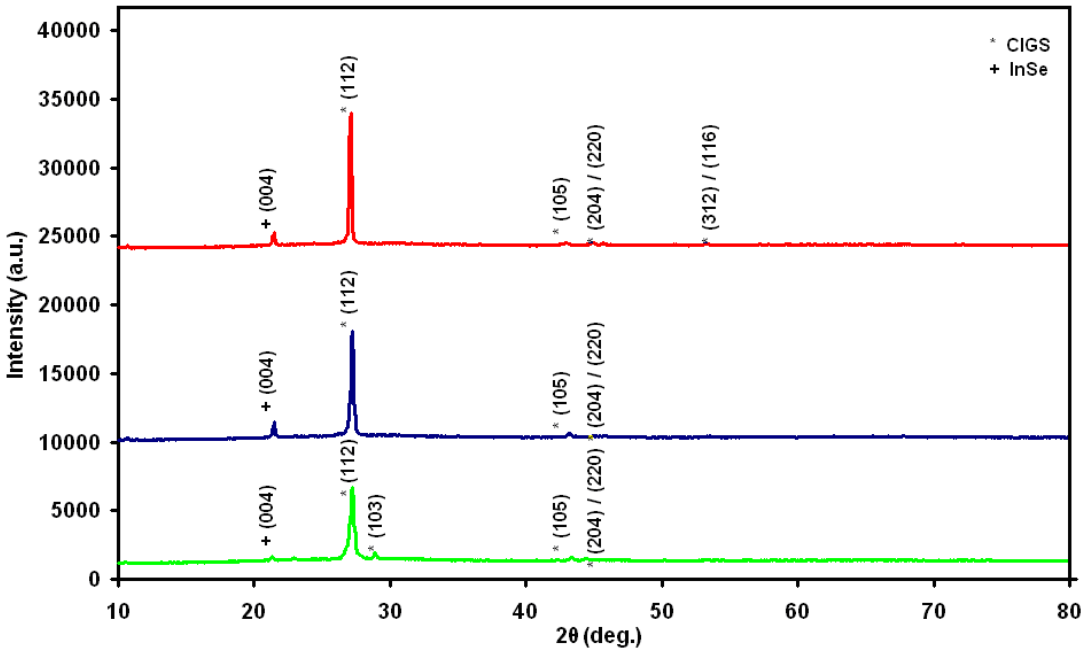

Figure 4.7 : X-ray diffraction patterns of CIGS thin films samples (S1) annealed at (a) 350 ^{o}C, (b) 400 ^{o}C, and (c) 450 ^{o}C for 30 minutes.

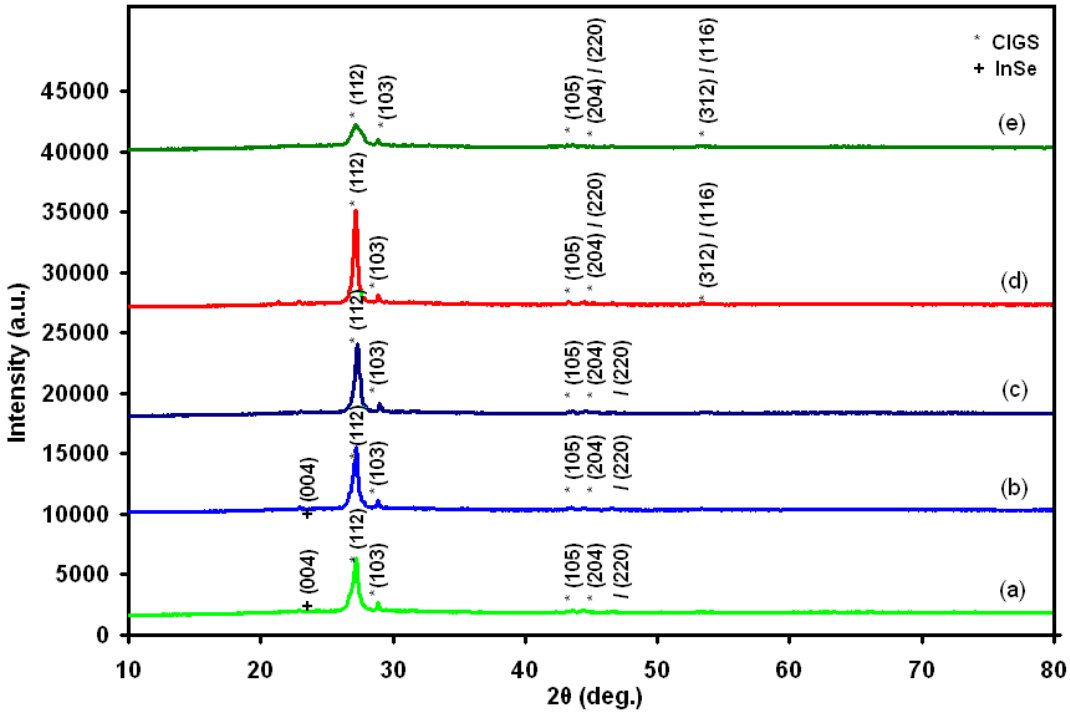

Figure 4.8 : X-ray diffraction patterns of CIGS thin film samples (S2 and S3) annealed at (a) 315 ^{o}C, (b) 330 ^{o}C, (c) 345 ^{o}C, (d) 360 ^{o}C for 5 minutes, (e) 315 ^{o}C for 15 minutes (S3).

Another group of samples were annealed between 300-360 ^{o}C with 15 ^{o}C steps in order to identify the critical annealing temperature and time for which the structure of film has the same form with the one for the S1 sample which was annealed at 350 ^{o}C. Specifically, S2 samples were annealed at 315, 330, 345 and 360 ^{o}C for 5 minutes and their XRD patterns are illustrated in Fig. 4.6. As shown in the figure, the XRD pattern of CIGS thin film did not change significantly with the increasing annealing temperature after 315 ^{o}C, but (312)/ (116) peak of CIGS appeared at the annealing temperature of 360 ^{o}C.

The third group of samples (S3) were annealed at the minumum annealing temperature of 315 ^{o}C for longer time, 15 minutes. The XRD pattern of a typical sample of this group was the same with the one for the sample annealed at 360 ^{o}C for 5 minutes.

In the following section the results of the characterization studies on two representative samples annealed at 315 ^{o}C for 15 minutes and at 450 ^{o}C for 30 minutes are discussed.

4.3.2 Energy Dispersive X-ray Analysis (EDXA) Results

Scanning electron microscopy (SEM) provides an information on the composition of near surface region and the high magnification image of the surface of material and the morfology of the material. The SEM images of CIGS thin films as given in Fig.4.9 showed uniform formation of the films with slight increase in the grain size with annealing. The compositions of the CIGS thin films were identified by means of the energy dispersive X-ray analysis (EDXA) measurements performed

simultaneously with SEM. The atomic percentage ratios of the elements are tabulated in the Table 4.3. As seen from the table the percentages of copper (Cu), and selenium (Se) increased and the atomic percentages of indium (In), and galium (Ga) in the samples decreased with annealing temperature.

The EDXA patterns are given for as-grown and annealed samples (S1 and S3) in Fig. 4.10, Fig. 4.11, and Fig. 4.12, respectively.

Table 4.3 : EDXA results of atomic ratio of as-grown and annealed CIGS thin films at different temperatures and time periods.

	Cu	**In**	**Ga**	**Se**
As-grown	16.24	28.25	11.57	43.93
Ann 315 ^{o}C - 15 min.(S3)	17.06	27.64	10.45	44.85
Ann 450 ^{o}C - 30 min.(S1)	18.74	25.01	10.87	45.38

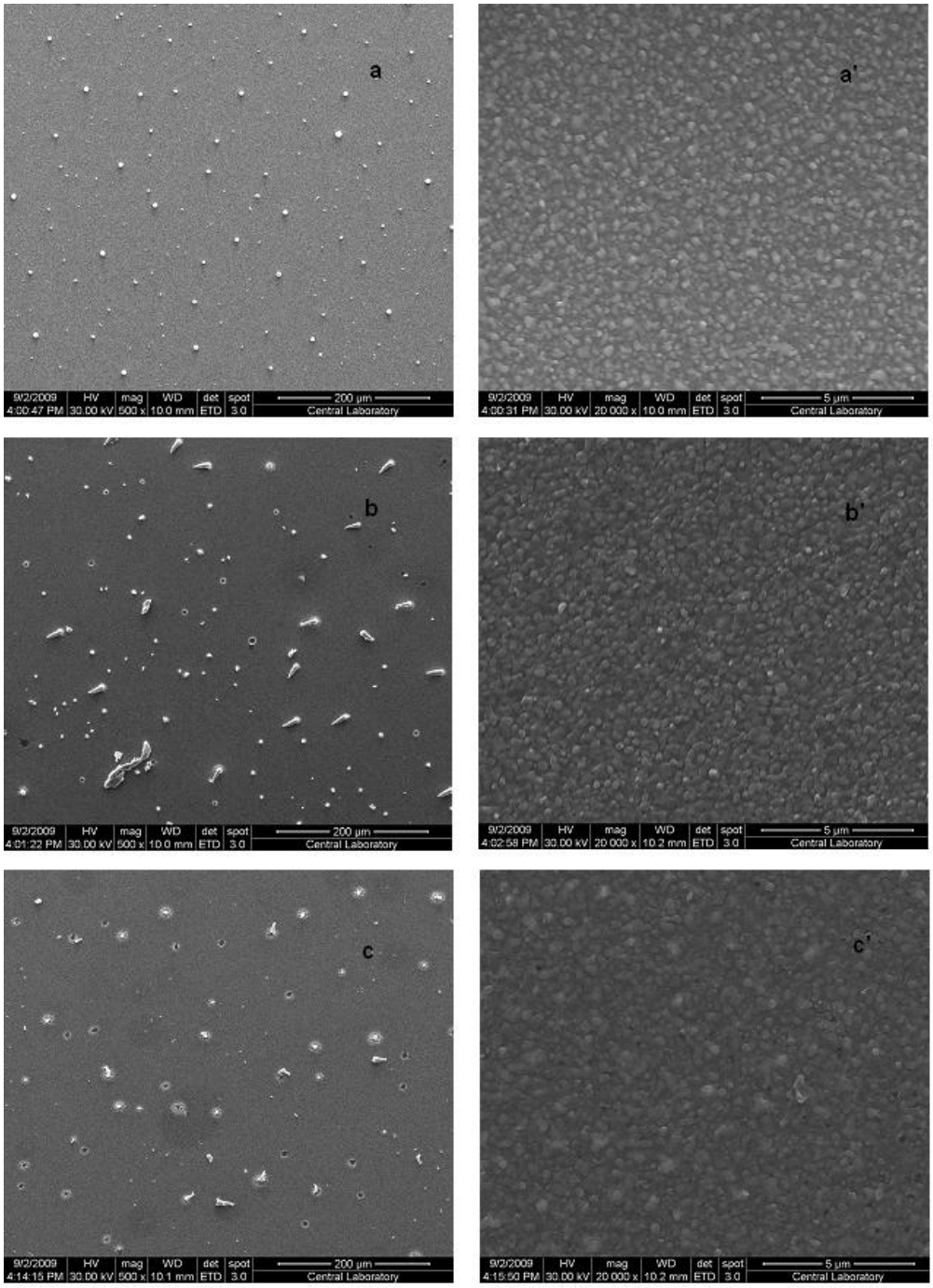

Figure 4.9 : SEM micrographs of CIGS thin films for (a) (a') as-grown, (b) (b') annealed 315 ^{o}C for 15 minutes (S3) and (c) (c') annealed at 450 ^{o}C for 30 minutes (S1).

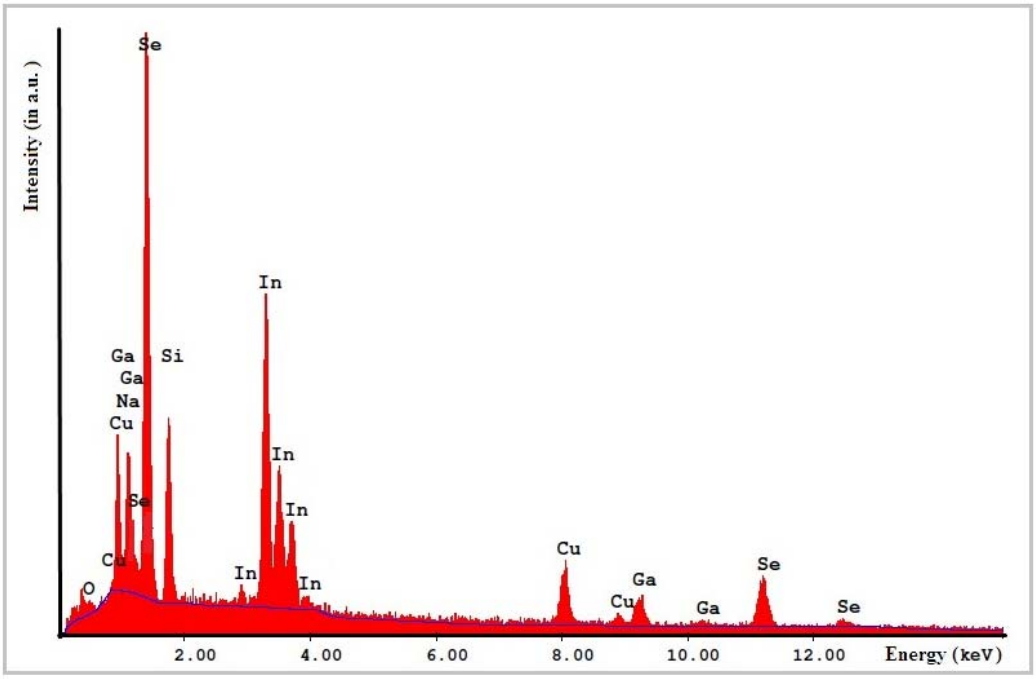

Figure 4.10 : The variation of intensity-dispersive energy obtained from EDXA analysis for as-grown CIGS thin film.

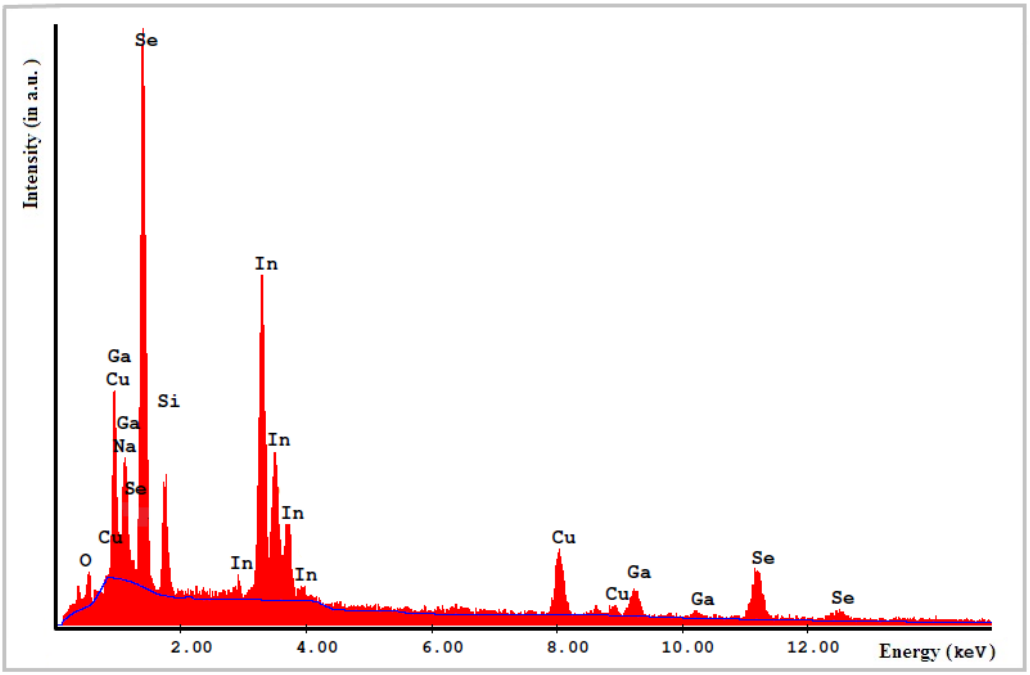

Figure 4.11 : The variation of intensity-dispersive energy obtained from EDXA analysis for annealed CIGS thin film (S3) at 315 ^{o}C for 15 minutes.

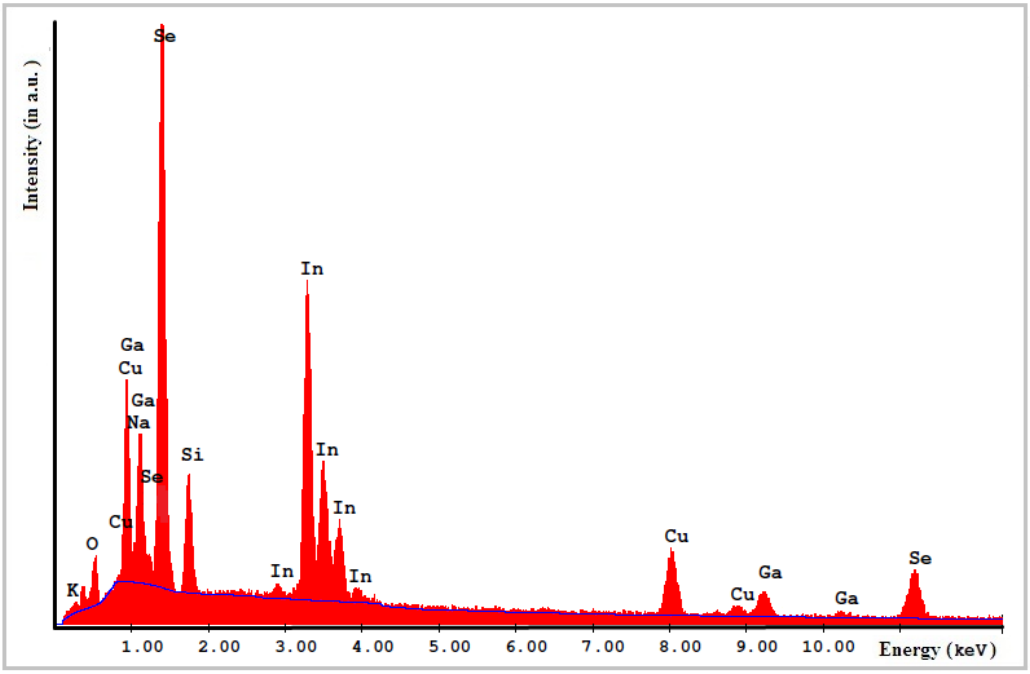

Figure 4.12 : The variation of intensity-dispersive energy obtained from EDXA analysis for annealed CIGS thin film (S1) at 450 ^{o}C for 30 minutes.

4.4 Electrical Characterization of CIGS Thin Films

In this section, the results of the electrical measurements performed on the as grown and annealed samples at 315 ^{o}C for 15 minutes and 450 ^{o}C for 30 minutes were presented.

For the electrical measurements, indium ohmic contacts were obtained by the evaporation of indium on the van der Pauw shape CIGS thin films using the suitable masks.

4.4.1 Conductivity Measurements

The room temperature conductivity values of the as grown and the annealed samples were measured to be in between 10^{-2} – $8x10^{-2}$ $(\Omega\text{-cm})^{-1}$; increasing with annealing temperature. In order to investigate the general behaviour of the conductivity, the temperature dependent conductivity measurements were performed in the temperature range 100 - 400 K for the as-grown and the annealed samples at 315 and 450 ^{o}C for 15 and 30 minutes respectively. Fig. 4.13 illustrates the variation of the electrical conductivity with reciprocal temperature. For all samples conductivity decreased with decreasing temperature at different rates in three different temperature regions.

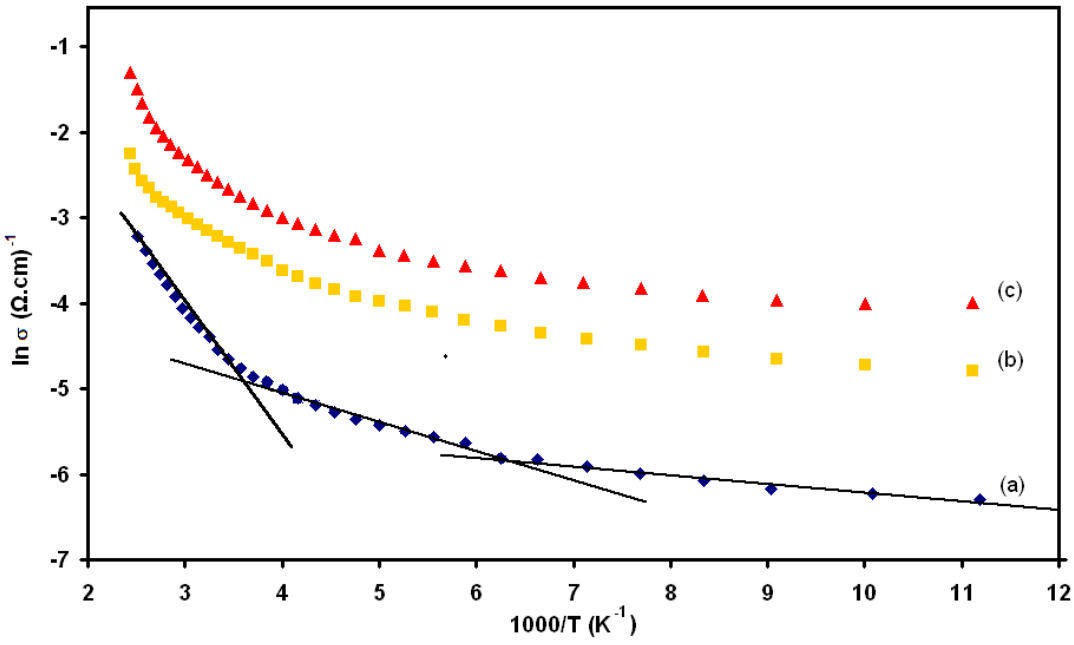

Figure 4.13 : The temperature dependent electrical conductivities of (a) as grown, and annealed CIGS thin films at (b) 315 ^{o}C for 15 minutes and (c) 450 ^{o}C for 30 minutes.

The variations of $ln\sigma$ vs T^{-1} showed three linear regions for all CIGS samples, with different activation energies (E_a). The activation energies calculated from the slopes of $ln\sigma$ vs T^{-1} for these three regions are given Table 4.4.

As seen from the Table 4.4, activation energies of 8.4 meV, 30.9 meV and 108.2 meV for as-grown ; 9.4 meV, 25.6 meV and 63.8 meV for annealed at 315 ^{o}C and 8.1 meV, 23.9 meV and 88.9 meV for annealed at 450 ^{o}C CIGS thin films, were obtained in the regions of 90-160, 170-250 and 260-400 K, respectively. The activation energy values are all less than the half band gap, indicating that not the intrinsic conduction, but the thermionic emission above 250 K dominated the electrical transport. Below 250 K the activation energy values are almost equal or less than kT; indicating that thermionic emission is not dominant.

Table 4.4 : The activation energy values of as grown and annealed CIGS thin films at 315 and 450 ^{o}C.

	Activation Energy (meV)		
Temp. Regions (K)	**As grown**	**Annealed at 315 ^{o}C 15 min. (S3)**	**Annealed at 450 ^{o}C 30 min. (S1)**
90-160	8.4	9.4	8.1
170-250	30.9	25.5	23.9
260-400	108.2	63.9	88.9

4.4.2 Carrier Concentration

Temperature dependent Hall effect and carrier concentration studies were performed in the temperature range of 100-400 K. The magnetic field was kept at a constant value of 0.97 T in the studied temperature range. Fig 4.14 illustrates the typical behavior of carrier concentration n as a function of temperature. Room temperature carrier concentration values of the films were found to be in the range of $5x10^{15}$ - $9x10^{15}$ cm^{-3} depending on the annealing temperatures.

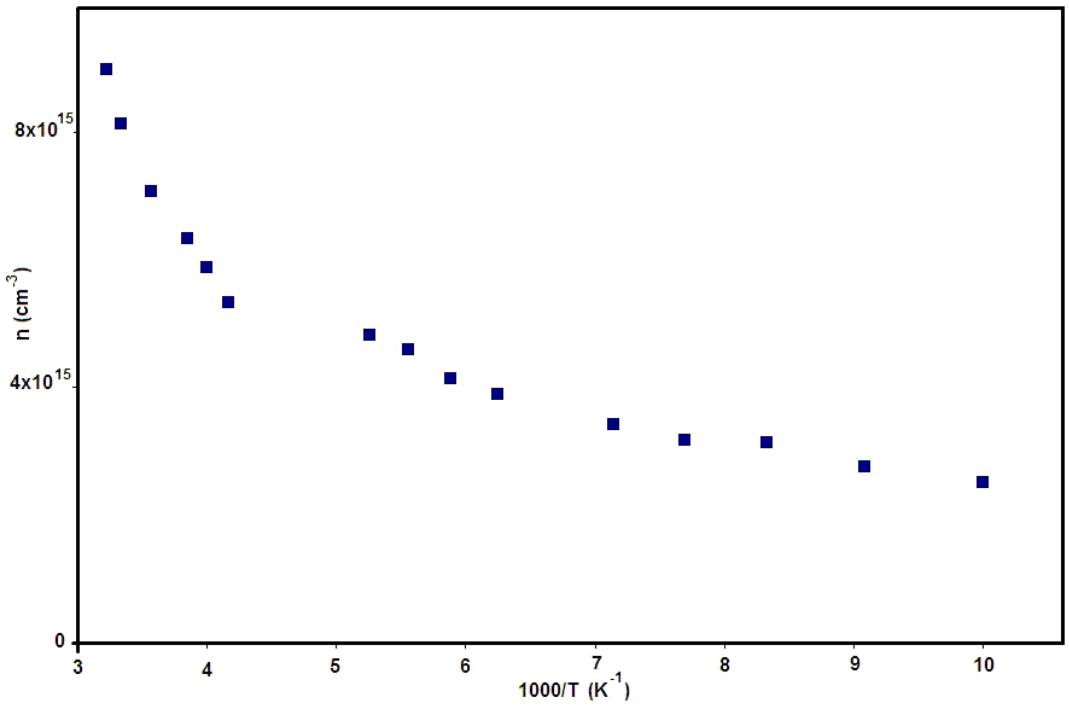

Figure 4.14 : The temperature dependent carrier density of CIGS thin film sample annealed at 315 ^{o}C for 15 minutes.

As illustrated in the Fig. 4.12, the carrier concentration decreases exponentially with decreasing ambient temperature at a higher rate in the high temperature region, where thermionic emission is the dominant conduction mechanism. However, in the low temperature region in between 100 - 250 K, temperature dependence of the carrier concentration is weak. For this typical sample; the room temperature mobility value was calculated as about 40 ($cm^2/V.s$) using Eq. 3.6.

4.5 Photoconductivity Analysis

The photoconductivity measurements were carried out as a function of illumination intensity in the temperature range of 100-400 K. The measurements were performed at different light intensities (Φ), which are 17, 34, 55, 81, and 113 mW/cm^2, and the illumination was provided by the halogen lamp. The variations of the photoconductivity as a function of reciprocal temperature (1000/T) in temperature range of 100-400 K are shown in Fig. 4.15, Fig. 4.16 and Fig. 4.17 for as-grown and annealed samples at 315 and 450 ^oC for 15 and 30 minutes respectively.

As it is clearly seen from the figures, the photoconductivity decreases with decreasing temperature and increases with increasing illumination intensity and at each illumination intensity the photoconductivity stays almost constant in the temperature range of 100-250 K. A considerable change in photoconductivity was observed above these temperatures.

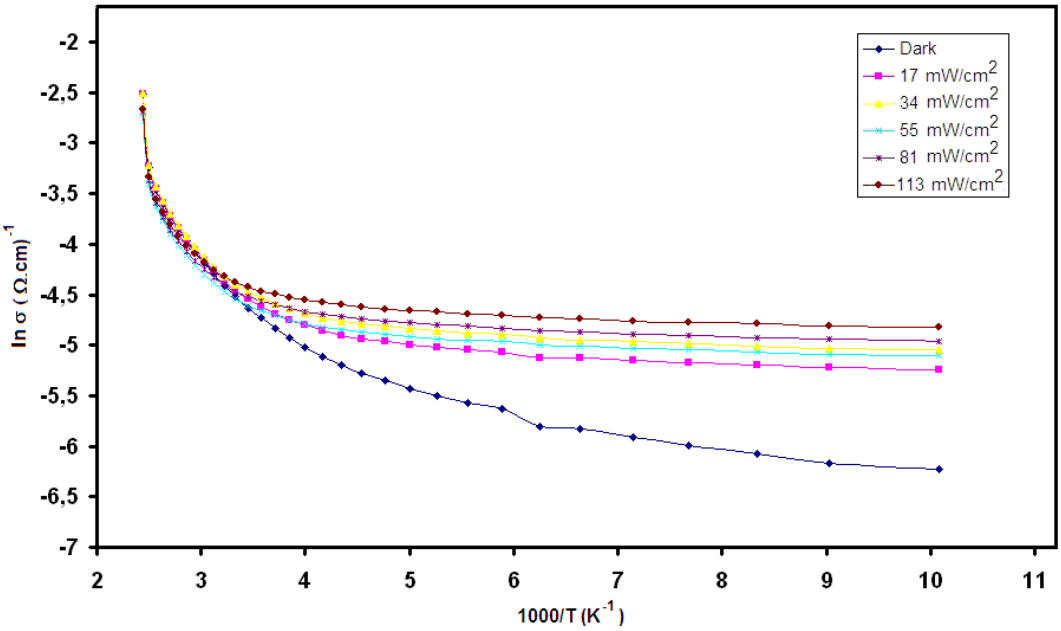

Figure 4.15 : The temperature dependent dark conductivity and photoconductivity of as-grown CIGS thin film sample.

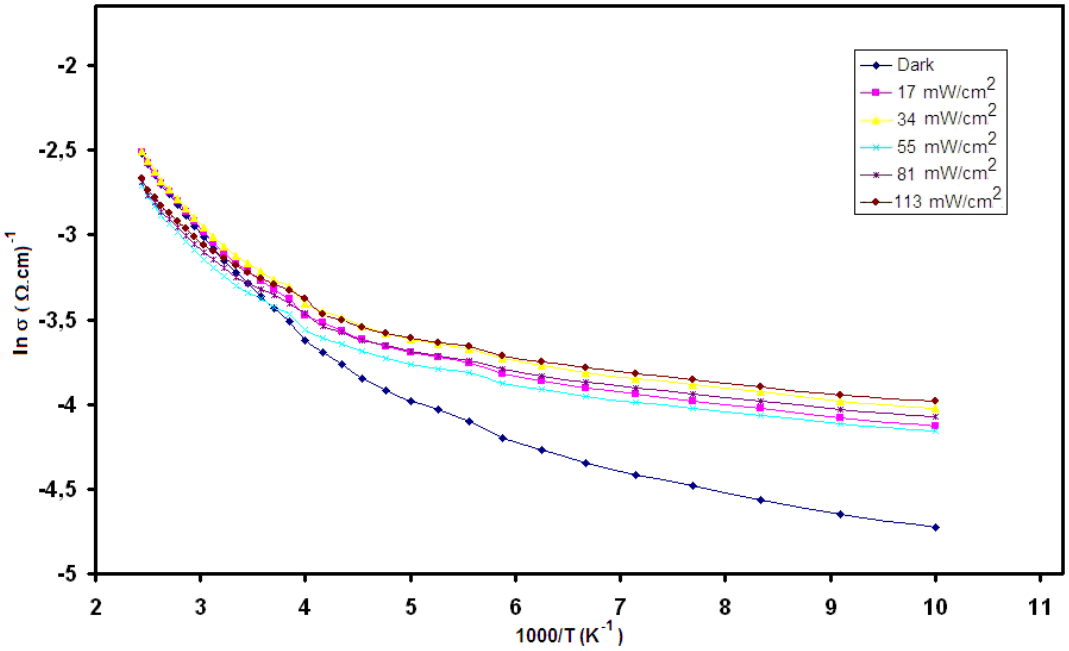

Figure 4.16 : The temperature dependent dark conductivity and photoconductivity of CIGS thin film sample annealed at 315 ^{o}C.

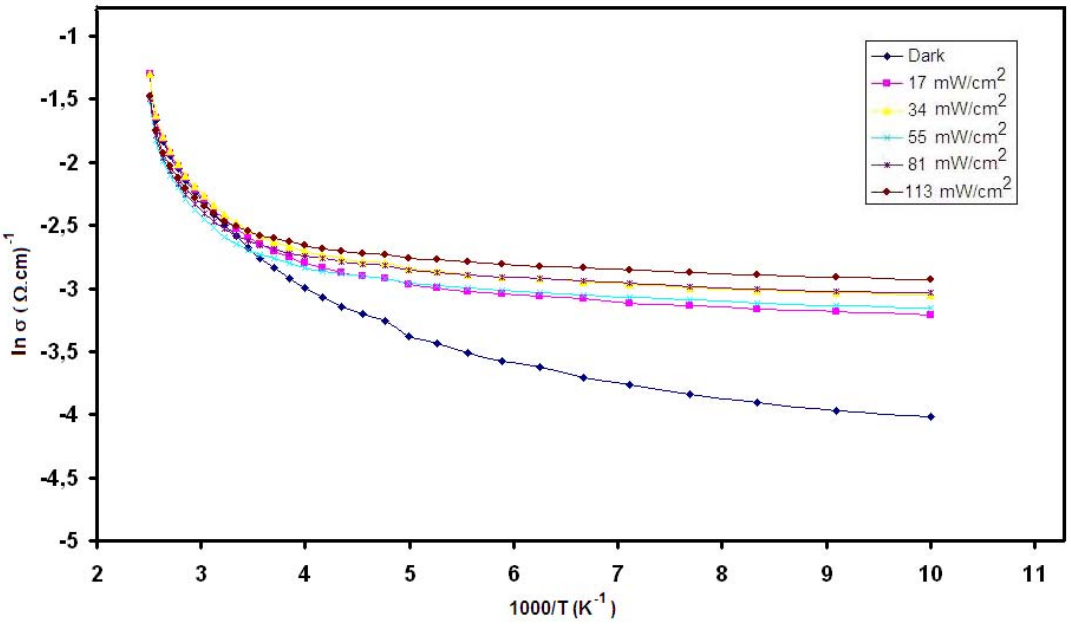

Figure 4.17 : The temperature dependent dark conductivity and photoconductivity of CIGS thin film sample annealed at 450 ^{o}C.

In order to determine the characteristics of the defects centers the photocurrent (I_{PC}) versus illumination intensity (Φ) was plotted in Log-Log scale at constant temperatures of 100, 200, 300 and 400 K for all samples as seen Fig. 4.13, Fig. 4.14 and Fig.4.15.

As illustrated in the figures, I_{PC} increases with increasing intensity. Photocurrent depends on illumination intensity as $I_{PC} \alpha \Phi^{n}$, here power exponent n was calculated from the slope of Log (I_{PC}) vs. Log (Φ). The case of $n<1$, corresponds to "*sublinear*" photoconductivity.

For the as grown CIGS thin film sample, the n values calculated from the slope of Fig. 4.16 and were found to be 0.20, 0.26, 0,44 and 0.53 for 100, 200, 300

and 400 K, respectively. For all temperatures, the values of *n* change between 0.20 and 0.53, which is an indication of the sublinear character of the photocurrent. From the slope of Fig.4.17 for the CIGS sample annealed at 315 ^{o}C, *n* values were found to be 0.16, 0.30, 0.37 and 0.48 for 100, 200, 300 and 400 K, respectively. These *n* values also indicate the sublinear photocurrent character. Finally, the n values for CIGS sample annealed at 450 ^{o}C were calculated from the slope of Fig. 4.18. The values of *n* were found to be 0.18, 0.23, 0.44 and 0.49 for 100, 200, 300 and 400 K, respectively. The character of photocurrent for this sample is sublinear like asgrown and annealed at 315 ^{o}C CIGS thin film samples. These results indicated that the sublinear character of photocurrent did not change with annealing.

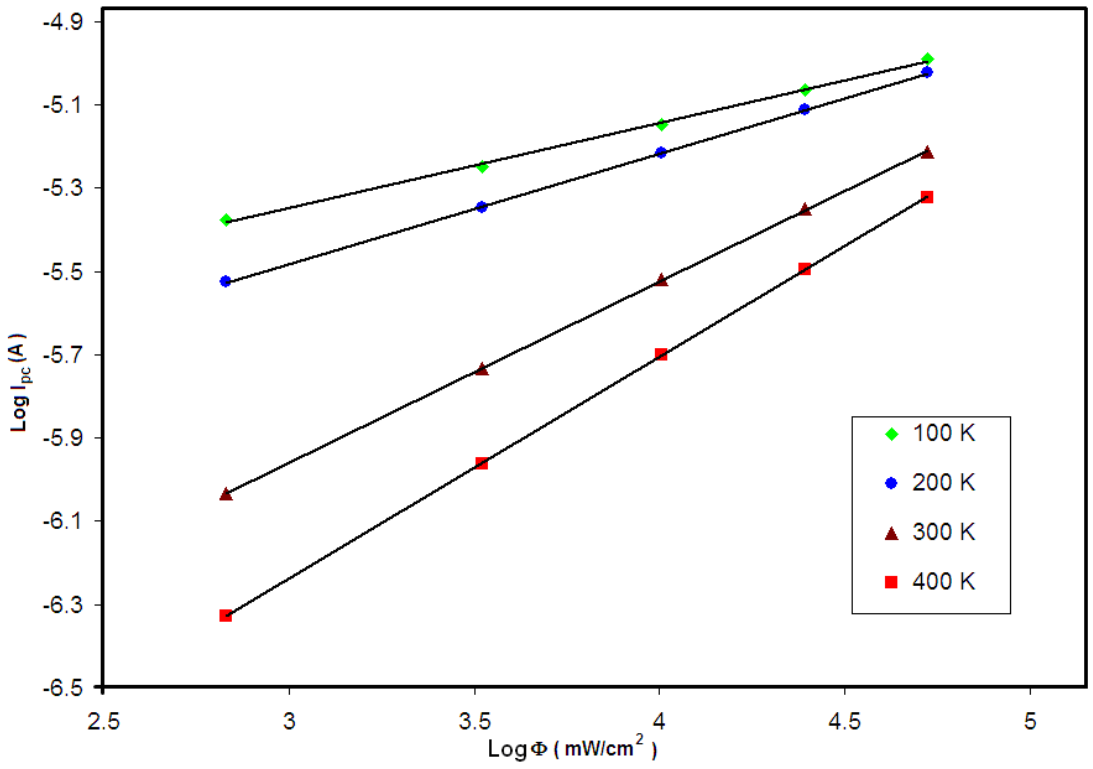

Figure 4.18 : Variation of Log I_{PC} – Log (Φ) at 100, 200, 300 and 400 K for asgrown CIGS thin film sample.

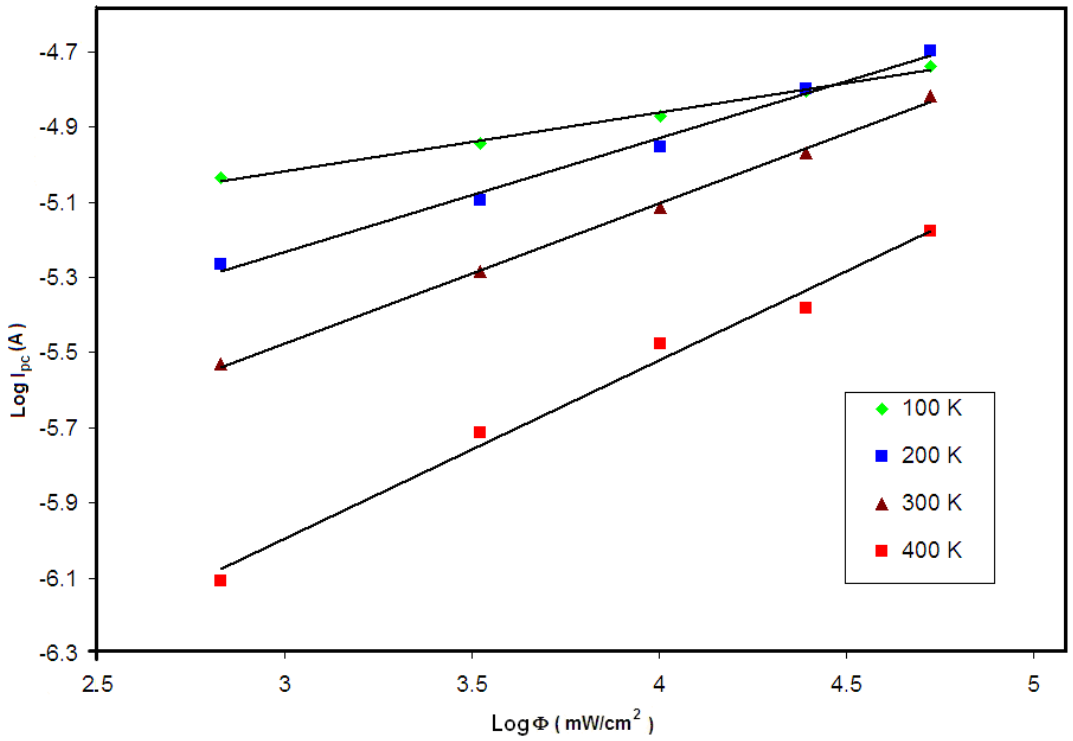

Figure 4.19 : Variation of Log I_{PC} – Log (Φ) at 100, 200, 300 and 400 K for CIGS thin film sample annealed at 315 ^{o}C.

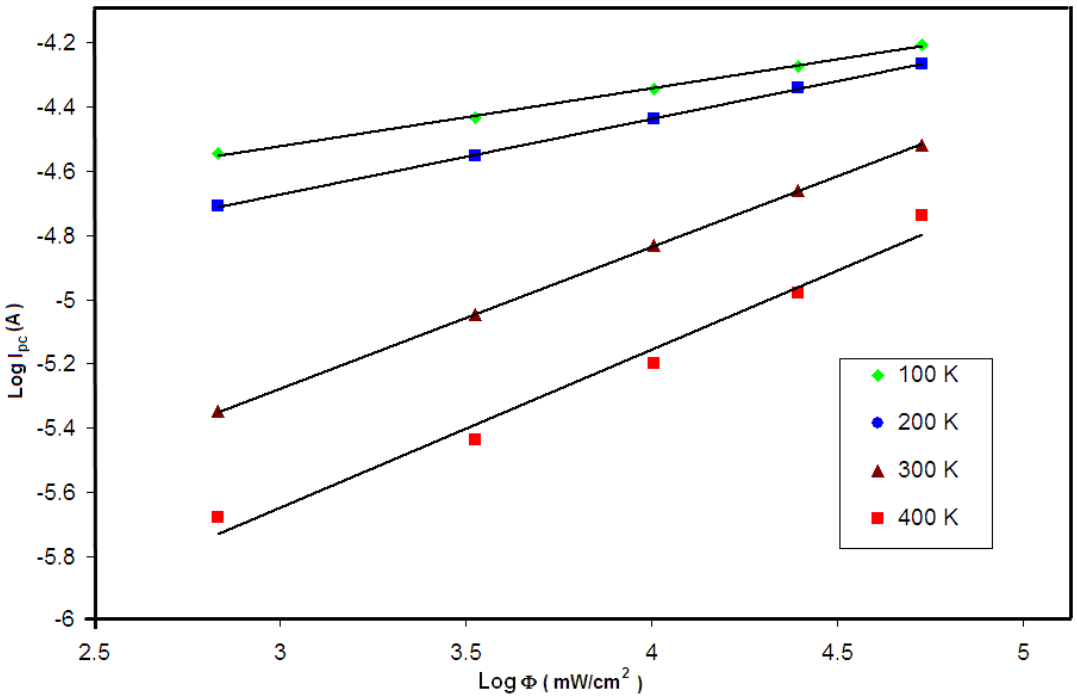

Figure 4.20 : Variation of Log I_{PC} – Log (Φ) at 100, 200, 300 and 400 K for CIGS thin film sample annealed at 450 ^{o}C.

4.6 Transmission and Absorption Measurements

This part of work has focused on the investigation of optical energy gap of the deposited CIGS thin films. The optical properties of CIGS thin films were examined to investigate the effect of growth method, parameters of growth, post annealing conditions and annealing time on the optical parameters. The transmission measurements were performed in the wavelength range of 325-900 nm. The optical absorption coefficient has been calculated from the transmission data using equation (2.33). The plot of $(\alpha h\upsilon)^2$ versus $(h\upsilon)$ for the as grown sample is shown in Fig. 4.21 which yielded a linear portion in the region of strong absorption near the absorption edge, indicating that absorption takes place through allowed direct interband transition. The optical band gap value was obtained from the extrapolation of the linear region with the energy axis, as 1.35 eV for as grown CIGS thin film. Transmission measurements were repeated after each annealing steps for all samples.

The optical band gap values were found to change in between 1.35 eV for as grown and annealed films at 315 ^{o}C for 15 minutes , and 1.41 eV for the films annealed at 450 ^{o}C for 30 minutes.

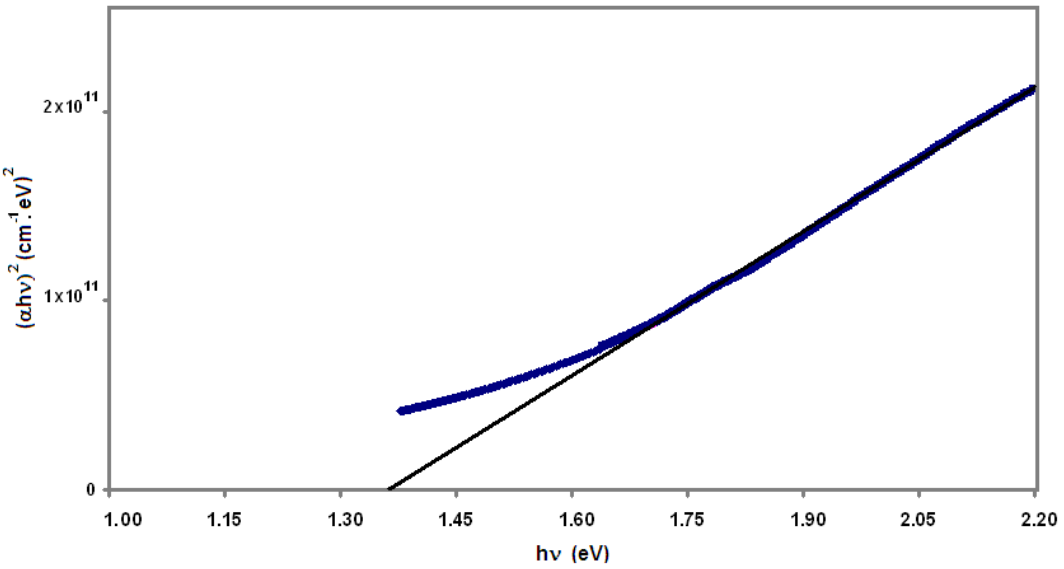

Figure 4.21 : The variation of absorption coefficient with photon energy (hυ) for asgrown CIGS thin film.

CHAPTER 5

CONCLUSIONS

The main purpose of this study was to characterize and analyze the structural, electrical and optical properties of the CIGS thin films deposited by e-beam and thermal evaporation methods onto the glass substrates for the possible application in solar cell device structures. The deposited films were subjected to different annealing procedures in order to get polycrystalline and stoichiometric thin films structures. Several e-beam and thermal evaporation runs were performed with the application of different deposition procedures and parameters, for the formation of stoichiometric films. It was observed that the successive layers of CIGS-Cu-CIGS, obtained by using double source e-beam evaporation technique, resulted polycrystalline $CuIn_{1-x}Ga_xSe_2$ thin film material. The detailed characterization studies were performed for these samples.

The structucal properties of the obtained CIGS thin films were examined by XRD and EDXA analysis. The identification of the peaks in the XRD spectra of the as grown and annealed samples (at 315, 330, 345 and 360 ^oC for 5 minutes at 300, 350, 400 and 450 ^oC for 30 minutes and at 315 oC for 15 minutes) under nitrogen atmosphere demonstrated that before and after annealing the films were polycrystalline in the nature with tetragonal chalcopyrite structure like the zinc blende having lattice parameters of a: 5.6 and c: 11.2 Å. Furthermore, XRD measurements indicated that the most intense peaks of all the deposited CIGS films

were around 26.7^{o} and the preferred crystalline orientation was in the direction of (112).

The compositional analysis carried out with the energy dispersive X-ray analysis (EDXA) showed that almost stoichiometric CIGS thin films were deposited on the substrates. However, a decrease in the indium (In) content and an increase in the selenium (Se), gallium (Ga) and copper (Cu) content were observed in the EDXA patterns as the annealing temperature increases.

Electrical conductivity measurements of the CIGS thin films were performed together with the effect of post depositional annealing. The temperature dependent conductivity measurements were carried out in the range of 100-400 K for as-grown and annealed samples at 315 and 450 ^{o}C. The room temperature conductivity of as grown and annealed films vary between 10^{-2} and $8x10^{-2}$ $(\Omega\text{-cm})^{-1}$ depending on the annealing temperatures and annealing times. The conductivity was observed to decrease with decreasing temperature with different rates in different temperature regions. The activation energies calculated from the slopes of the $\ln(\sigma)$-T^{-1} plots as 8.4 meV, 30,9 meV and 108,2 meV for as-grown sample, 9.3 meV, 25,5 meV and 63,8 meV for annealed samples at 315 ^{o}C and 8.1 meV, 23,9 meV and 88.8 meV for annealed one at 450 ^{o}C; in the corresponding temperature regions 90-160, 170-250 and 260-400 K, respectively. These results indicated that the dominating transport mechanism above 250 ^{o}C is thermionic emission.

The room temperature carrier concentrations of the films were found to be in the range of $5x10^{15}$ - $9x10^{15}$ cm^{-3} depending on the annealing temperatures and annealing times. The carrier concentration decreases exponentially with decreasing temperature in the high temperature region due to thermionic emission. All the

deposited thin film samples exhibited n-type conduction, defined by hot probe technique.

The photoconductivity measurements of as grown and annealed films at 315 and 450 ^{o}C were performed as a function of illumination intensity in the studied temperature range of 100-400 K. The photoconductivity varies with temperature and increases with increasing illumination intensity. The photoconductivity stays almost constant in the temperature range of 100-260 K for all illumination intensity values. Above this temperature range, the photoconductivity varies gradually with temperature and increases with increasing illumination intensity. From the variation of the photocurrent as a function of illumination intensity at temperatures of 100, 200, 300, and 400 K; n value in the $I_{PC} \alpha \Phi^{n}$ relation, was obtained in between 0.16 and 0.53 for these constant temperatures. According to the theory, $n \leq 1$ gave the indication of the sublinear character of the photocurrent.

The optical band gaps values of the as grown and annealed thin film samples were determined through transmission measurements. The absorption coefficient decreases exponentially with decreasing photon energy. The room temperature absorption coefficient values were found to be in the range of 10^{5}-10^{6} cm^{-1} for the incident photon energies between 1.37 – 3.81 eV. The optical band gap values were obtained as 1.35 eV and 1.41 eV for the asgrown and annealed samples at 450 ^{o}C.

In this study, polycrystalline thin films of $CuIn_{1-x}Ga_{x}Se_{2}$ with the optical band gap of 1.35 eV, n-type conductivity of 10^{-2} $(\Omega\text{-cm})^{-1}$ were deposited by the e-beam technique. The growth of stoichiometric p-type CIGS thin films with lower conductivity values for the solar cell application, is the aim of the near future study.

REFERENCES:

[1] M. Ohring, *Material Science of Thin Film*, 2nd. Edition,Academic Press,San Diego, 2002

[2] V.Smil *"General Energetics*: *Energy in the Biosphere and Civilization*." NewYork: John Wiley & Sons, 1991

[3] N.S. Lewis Science 315, p.798, (2007).

[4] E. Becquerel. Comptes Rendues Acad Sci. 9, p. 561, (1839).

[5] W.Smith, J. of the Soc. Telegraph Engineers, vol.2, no.1, p. 711-714, (1873).

[6] J. Wennerberg, Design and Stability of Cu(In,Ga)Se_2-Based Solar Cell Modules, Acta Universitatis Upsaliensis, Uppsala, 2002.

[7] S.-H Wei, S.B. Zhang, A. Zunger, Applied Physics Letters; 72: p.3199-3201, 1998.

[8] M. Venkatachalam, M.D. Kannan, S. Jayakumar, Thin Solid Films, Vol.516, Issue 20, (2008).

[9] K. Ramanathan, G. Teeter, J.C. Keane and R. Noufi, Thin Solid Films, Vol.480-481, (2005).

[10] R. Caballero and C. Guillén, Thin Solid Films, Vol.431-432, (2003).

[11] T.J. Gillespie, W.A. Miles, J.A. del Cueto, " *Photovoltaic Specialists Conference,* p.487-490,(1997)

[12] M. Klenk, O. Schenker, V. Alberts and E. Bucher, Semicond. Sci. Technol., Vol.**17,** No;5, p. 435-439, (2002).

[13] F. Smaili, M. Kanzari, B. Rezig, Materials Sci. and Engineering, Vol.28 Issue 5-6, p. 954–958, (2008).

[14] E. Niemi, J. Hedstrom, T. Martinsoy *et al* ,25th PVSC; Washington,D.C. (1996)

[15] B. M. Başol, A. Halani,C. Leidholm, G. Norsworthy, V. K. Kapur, A. Swartzlander ,Prog. Photovolt. Res. Appl., Vol.8, p.227-235, (2000).

[16] K. Kushiya, A. Shimizu, A. Yamada, M. Konagia, Jpn. J. Appl.Phys., Vol.34, p.54-60, (1995).

[17] E. Ahmed, R.D. Tomlinson, R.D. Pilkington, A.E. Hill, W. Ahmed, N. Ali, I.U. Hassan, Thin Solid Films, Vol.335, Issue 1- 2, (1998).

[18] P. Luo, G. Jianga, C. Zhua, Chinese Jou. of Chem. Phys. Vol.22, (2009).

[19] K. Matsubara, P. Fons, K. Iwata, A. Yamada, K. Sakurai, H. Tampo and S. Niki, Thin Solid Films, Vol.**431**, p.369, (2003).

[20] R. N. Bhattacharya, W. Batchelor, J. F. Hiltner and J. R. Sites. App. Phys. Lett., Vol.75, Issue 10, p.1431, (1999).

[21] J. H. Werner, J. Mattheis, U. Rau, Thin Solid Films, Vol.480 - 481, p.339 -409 , (2005).

[22] F. LONG, W. WANG1, J. DU, Z. ZOU, Journal of Physics: Conference Series, Vol.152, 012074, (2009)

[23] J.C.C. Fan, B-Y. Tsaur, and B.J. Palm, Conference Record of the 16th IEEE Photovoltaics Specialists Conference, New York, p. 692, (1982).

[24] N.B. Chaure, A.P. Samantilleke, R.P. Burton, J. Young, I.M. Dharmadasa, Thin Solid Films, Vol.472, p.212– 216, (2005).

[25] S.M. Sze, Know K., Physics of Semiconductor Devices, Third Ed. New Jersey, 2007

[26] Contreras MA, Egaas B, Ramanathan K, Hiltner J, Swartzlander A, Hasoon F, Noufi R., Progress in Photovoltaics Research and App. Vol.7, p.311–316, 1999.

[27] S. Ishizuka, K. Sakurai, A. Yamada, *K*. Matsubara, P. Fons, K. Iwata, S. Nakamura, Y. Kimura, T. Baba, H. Nakanishi, T. Kojima, S. Niki, Solar Energy Materials & Solar Cells, Vol.87, p.541–548, 2005.

[28] C. H. Champness, Proceedings of the 29th IEEE Conference (IEEE, Piscataway,NJ, 2002), p. 732; L. S. Yip and I. Shih, Proceedings of the First World Conference on Photovoltaic Energy Conversion, p. 210-213. IEEE, Piscataway, NJ, 1994.

[29] R.M. Burgess, W.S. Chen, W.E. Devaney, D.H. Doyle, N.P. Kim, and B . J . Stanbery, Conference Record of the 20th IEEE Photovoltaics Suecialists Conference (IEEE, New York, 1988) p.909.

[30] S.B.Zhang, S.-H. Wei, A. Zunger, Phys. Rev. B 57 : p.9642–9656, 1998.

[31] S.-H Wei, S.B. Zhang, A. Zunger, Applied Physics Letters; 72: p.3199-3201, 1998.

[32] D.S. Albin, J.R. Tuttle, G.D. Mooney, J.J. Carapella, A.Duda, A.Mason, and R. Noufi, Proceedings of the 21st IEEE photovoltaic specialists conferance, p. 562-569, 1990.

[33] J. E. Jaffe and A. Zunger, Phys. Rev. B 28: p. 5822-5847, 1983.

[34] M. I. Alonso, M. Garriga, C. A. Durante Rincön, E. Hernández, and M. León, Applied Phys. A : Mater. Sci. Process, 74: p. 659-664, 2002.

[35] C. Kittel, *Introduction to Solid State Physics*, 8th Edition, John Willey&Sons, 2005.

[36] H. Karaağaç, MS thesis, METU, Ankara, 2005.

[37] E.H. Hall, Am. J. Math. 2, 287 (1879).

[38] K.F. Brennan, A.S. Brown, *Theory of Modern Electronic Semiconductor Devises*, Wiley&Sons, Inc.,2002.

[39] R. H. Bube, *Photoconductvity of Solids*, John Willey & Sons, Inc. New York , 1960.

[40] B.G. Yacobi, "Semiconductor Materials", Kluwer Academic/Plenum Publishers, Newyork, Boston, Dordrecth, London, Moscow, 2002

[41] Oxford Vacuum Science, *http://www.oxford-vacuum.com/background/thin_film /evaporation.htm* , last visited on December 9, 2009.

[42] J. Yeager and M. A. Hrusch-Tupha, "*Low level measurements*", Ohio, Keithley Instruments. Inc. (1998).

[43] N. F. Mott and E. A. Davis, "*Electronic Process in Noncrystalline Materials"*, Clarendan press, Oxford, (1971).

[44] M.A.Contreras, M.J.Romero, R.Noufi, *Thin Solid Films*,511–512, 51– 54, 2006.

[45] N.G. Dhere, S. S. Kulkarni, A. H. Jahagirdar, A. A. Kadam, *Journal of Physics and Chemistry of Solids,* Vol.66, p.1876–1879, 2005.